




# The key protein of endosomal mRNP transport Rrm4 binds translational landmark sites of cargo mRNAs

Lilli Olgeiser<sup>1</sup>, Carl Haag<sup>1</sup>, Susan Boerner<sup>2</sup>, Jernej Ule<sup>3,4</sup> , Anke Busch<sup>5</sup>, Janine Koepke<sup>6</sup>, Julian König<sup>5</sup>, Michael Feldbrügge<sup>1,\*</sup>  & Kathi Zarnack<sup>2,\*\*</sup> 

## Abstract

RNA-binding proteins (RBPs) determine spatiotemporal gene expression by mediating active transport and local translation of cargo mRNAs. Here, we cast a transcriptome-wide view on the transported mRNAs and cognate RBP binding sites during endosomal messenger ribonucleoprotein (mRNP) transport in *Ustilago maydis*. Using individual-nucleotide resolution UV crosslinking and immunoprecipitation (iCLIP), we compare the key transport RBP Rrm4 and the newly identified endosomal mRNP component Grp1 that is crucial to coordinate hyphal growth. Both RBPs bind predominantly in the 3' untranslated region of thousands of shared cargo mRNAs, often in close proximity. Intriguingly, Rrm4 precisely binds at stop codons, which constitute landmark sites of translation, suggesting an intimate connection of mRNA transport and translation. Towards uncovering the code of recognition, we identify UAG as specific binding motif of Rrm4 that is bound by its third RRM domain. Altogether, we provide first insights into the positional organisation of co-localising RBPs on individual cargo mRNAs.

**Keywords** endosome; fungus; iCLIP; RNA transport

**Subject Categories** Membrane & Intracellular Transport; RNA Biology

**DOI** 10.15252/embr.201846588 | Received 14 June 2018 | Revised 9 November 2018 | Accepted 9 November 2018 | Published online 14 December 2018

**EMBO Reports (2019) 20: e46588**

## Introduction

All eukaryotic cells must accurately regulate the expression of proteins in time and space. To this end, many mRNAs accumulate at specific subcellular sites, and their local translation is exactly timed [1–3]. mRNA localisation is achieved most commonly by

active motor-dependent transport along the cytoskeleton. Functional transport units are messenger ribonucleoprotein complexes (mRNPs), consisting of various RNA-binding proteins (RBPs), accessory proteins and cargo mRNAs. Key factors are RBPs that recognise localisation elements (LEs) within mRNAs. For movement, the RBPs either interact with motors directly or are connected via linker proteins [1,4].

We discovered co-transport of mRNPs on the cytoplasmic surface of early endosomes as a novel translocation mechanism of cargo mRNAs during hyphal growth in fungi [5,6]. These endosomes shuttle along microtubules by the concerted action of plus-end-directed kinesin and minus-end-directed dynein [7,8]. They serve as multi-purpose platforms functioning not only during endocytic recycling but also during long-distance transport of whole organelles such as peroxisomes [9–12].

Endosomal mRNA transport was uncovered analysing the RBP Rrm4 in the dimorphic phytopathogenic fungus *Ustilago maydis* (Fig EV1A) [13,14]. Loss of Rrm4 has no effects on the yeast form of the fungus. However, the absence of Rrm4 causes characteristic defects in unipolar growth when switching to the hyphal form: the fraction of bipolarly growing hyphae increases and the insertion of basal septa is delayed [6,15]. In line with endosomal mRNA transport, Rrm4 binds mRNAs and shuttles on early endosomes along microtubules *in vivo* [5,16]. Using the poly(A)-binding protein Pab1 as an mRNA marker revealed that loss of Rrm4 abolishes this transport, resulting in a gradient of mRNAs declining from the nucleus towards the cell periphery [17]. Thus, one function of Rrm4 might be the general distribution of mRNAs within hyphae [17].

Initial CLIP experiments with Rrm4 identified target mRNAs encoding chitinase Cts1 and septin Cdc3, among others [17,18]. The subcellular localisation of both proteins was Rrm4-dependent: loss of Rrm4 strongly reduced the secretion of the chitinase Cts1. Moreover, shuttling of the Cdc3 protein on early endosomes was

1 Institute for Microbiology, Cluster of Excellence on Plant Sciences, Heinrich Heine University Düsseldorf, Düsseldorf, Germany

2 Buchmann Institute for Molecular Life Sciences (BMLS), Goethe University Frankfurt, Frankfurt am Main, Germany

3 The Francis Crick Institute, London, UK

4 Department of Molecular Neuroscience, UCL Institute of Neurology, London, UK

5 Institute of Molecular Biology gGmbH, Mainz, Germany

6 Medical Clinic II (Molecular Pneumology), Excellence Cluster Cardio-Pulmonary System, Justus Liebig University of Gießen, Gießen, Germany

\*Corresponding author. Tel: +49 211 81 15475; E-mail: feldbrue@hhu.de

\*\*Corresponding author. Tel: +49 69 798 42506; E-mail: kathi.zarnack@bmls.de

abolished, and the gradient of septin filaments at the growth pole of hyphae was no longer formed [6]. Since *cdc3* mRNA and its encoded protein are found together with ribosomes on the same shuttling endosomes, we hypothesised that endosome-coupled translation of *cdc3* mRNA during long-distance transport is critical for the efficient formation of septin filaments at the growth pole [6]. This was supported by demonstrating that all four septin-encoding mRNAs are present on endosomes and that septin proteins assemble into heteromeric complexes on the cytoplasmic face of endosomes during long-distance transport [19]. Thus, Rrm4-dependent mRNA transport regulates the specific localisation of the corresponding translation products. To understand this complex process at the transcriptome-wide level, we present herein an *in vivo* snapshot of RNA binding sites of endosomal RBPs on cargo mRNAs at single nucleotide resolution.

## Results

### Loss of the glycine-/glutamine-rich protein Grp1 affects hyphal growth

In order to identify additional protein components involved in endosomal mRNA transport, we performed pilot affinity tag purification using Rrm4 as bait. We identified the potential RBP glycine-rich protein 1 (Grp1; UMAG\_02412), which carries an N-terminal RNA recognition motif (RRM) domain followed by a short C-terminal region rich in glycine and glutamine (GQ-rich; Figs 1A and EV1B–D). The protein was similar to other small RRM proteins, such as human CIRBP or RBM3 and plant RBG7 (AtGRP7), all previously described as global stress regulators (Fig 1A) [20,21].

For functional analysis, we generated deletion mutants in laboratory strain AB33. In this strain, the master transcription factor controlling hyphal growth is under control of an inducible promoter. Thus, hyphal growth can be elicited synchronously by changing the nitrogen source in the medium. The corresponding hyphae grow like wild type by tip expansion at the apical pole, while the nucleus is positioned in the centre and septa are inserted in regular intervals at the basal pole (Fig EV1A) [22]. In the yeast form of AB33, we observed that loss of Grp1 resulted in slower proliferation as well as increased cell size (Fig EV1E–G). At lower temperatures, growth of the *grp1Δ* strain was affected even more strongly and it exhibited an altered colony morphology (Fig EV1H). This was consistent with a potential function in cold stress response, similar to the plant and human orthologues [20,21]. Furthermore, colony growth of the *grp1Δ* strain was strongly reduced upon treatment with inhibitors of cell wall biosynthesis, such as calcofluor-white (CFW) or Congo red (CR) [23,24]. Hence, loss of Grp1 might cause defects in cell wall formation (Fig EV1I).

Studying hyphal growth revealed that, unlike observed in *rrm4Δ* strains, loss of Grp1 did not cause an increased amount of bipolar cells as it is characteristic for defects in microtubule-dependent transport (see *rrm4Δ* hyphae for comparison; Fig 1B and C) [12]. On the contrary, under optimal growth conditions hyphae were significantly longer (Fig 1B and C), and the length of empty sections at the basal pole was increased (Figs 1D and EV1J). Hence, the coordination of hyphal growth may be disturbed in the absence of

Grp1. In order to further investigate this, we stressed hyphae 3 hours post-induction (h.p.i.) of hyphal growth with the cell wall inhibitor CFW. In comparison with wild type hyphae, we observed a strongly increased number of *grp1Δ* hyphae with abnormal shapes (86%), indicating that cell wall integrity might be affected (Fig 1E and F).

In summary, loss of Grp1 affects both yeast-like and hyphal growth. During the latter, Grp1 seems to be crucial for the correct coordination of cell wall expansion, which becomes particularly apparent during stress conditions.

### Grp1 is a novel component of endosomal mRNA transport

To analyse the subcellular localisation of Grp1, we generated AB33 strains expressing Grp1 fused at its C-terminus to Gfp by homologous recombination. The functional Grp1-Gfp version accumulated in the cytoplasm as well as in the nucleus of hyphae. In comparison, the poly(A)-binding protein Pab1-Gfp was absent from the nucleus, suggesting that this localisation pattern is specific for Grp1 (Fig 2A). Importantly, a subpopulation of Grp1-Gfp moved bi-directionally in the cytoplasm with a velocity comparable to Rrm4-Gfp and Pab1-Gfp, which are known to shuttle on early endosomes (Fig 2A and B; Video EV1).

To test whether Grp1 shuttles on Rrm4-positive endosomes, we performed dynamic co-localisation studies using dual-view technology [25]. We generated AB33 strains co-expressing Grp1-Gfp and Rrm4 fused C-terminally to the red fluorescent protein tag-Rfp (tRfp) [26]. For comparison, we used a strain expressing Pab1 fused to the red fluorescent protein mCherry [17,27]. Analysing hyphae 6 h.p.i. 99% of processive Grp1-Gfp signals co-migrated with Rrm4-tRfp, revealing extensive co-localisation of both proteins in shuttling units (Fig 2C and D; Video EV2). Consistently, 97% of processive Grp1-Gfp signals co-migrated with Pab1-mCherry, indicating that Grp1, like Pab1, was present on Rrm4-positive endosomes (Fig 2C and D; Videos EV3 and EV4). Thus, Grp1 appears to be a novel component of endosomal mRNPs that might already be recruited to transport mRNPs in the nucleus.

### The endosomal localisation of Grp1 depends on Rrm4

To investigate whether Grp1 has an influence on the shuttling of Rrm4-positive endosomes, we studied Rrm4 movement in *grp1Δ* strains. Loss of Grp1 altered neither processive Rrm4-Gfp movement nor the velocity of the respective endosomes (Fig 2E and F; Video EV5). Vice versa, studying Grp1-Gfp movement in the absence of Rrm4 revealed that its endosomal localisation depended on Rrm4 (Fig 2G). Importantly, similar to Pab1-Gfp, a gradient of Grp1-Gfp was formed in *rrm4Δ* hyphae, with a decreasing signal intensity towards the growing apex (Fig 2H and I) [17]. Similar to Pab1, which is expected to associate with almost all poly(A) tails of mRNAs [28], Grp1 might therefore be distributed in association with many mRNAs (see below).

To test whether Grp1-Gfp binds to endosomes in an mRNA-dependent manner, we generated AB33 strains expressing Rrm4<sup>mR123</sup>-tRfp. This Rrm4 variant carried point mutations in the RNP1 regions of RRM domains 1–3 causing a reduced RNA binding activity and loss of function of Rrm4 [16]. In dual-view experiments, we observed that Grp1-Gfp like Pab1-Gfp no longer shuttled in the

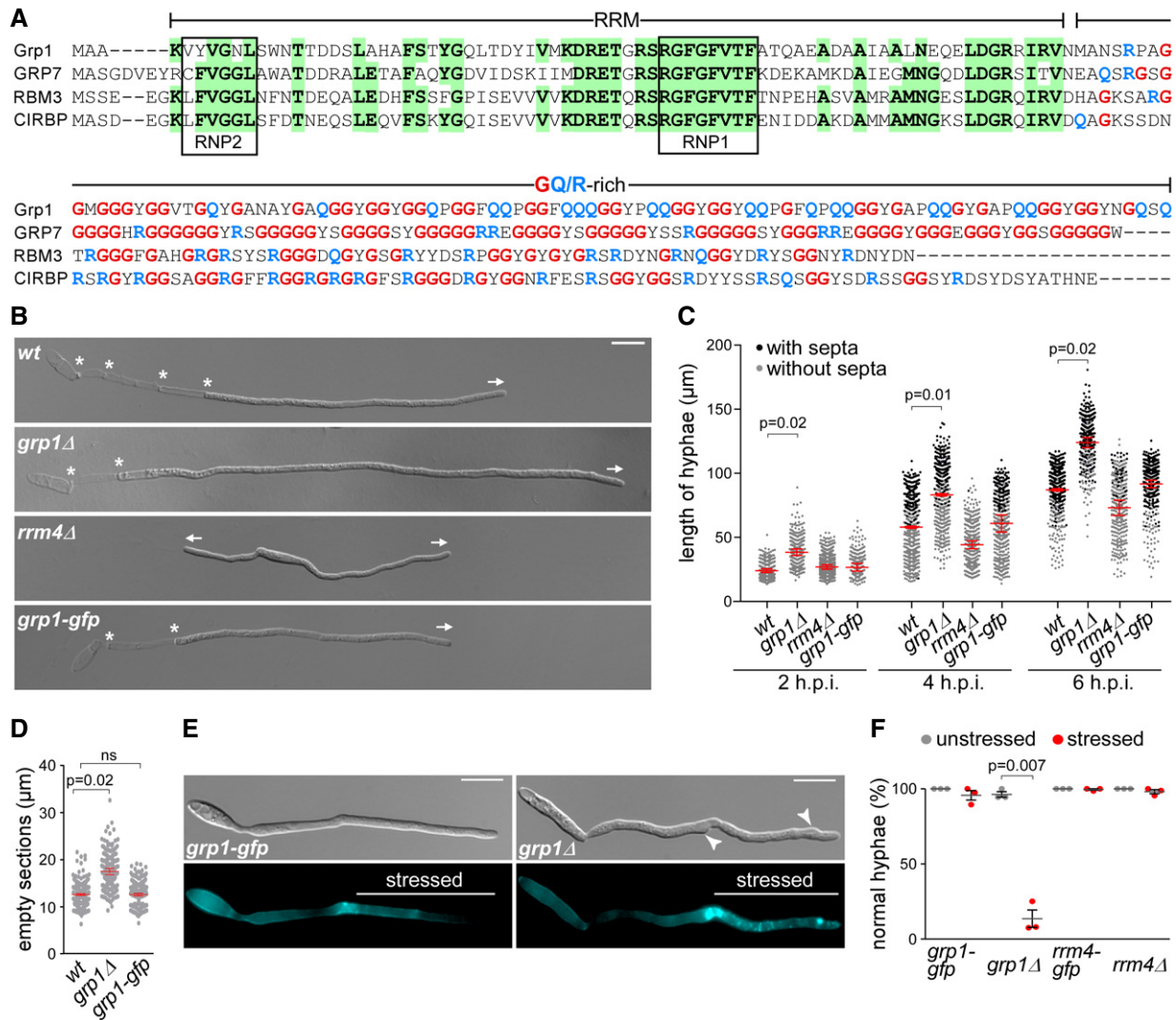


**Figure 1. Grp1 is important for hyphal growth under suboptimal conditions.**

**A** Sequence alignment of glycine-rich proteins (Fig EV1B). *UmGrp1* from *U. maydis* (UMAG\_02412), *AtGRP7* (RBG7) from *A. thaliana* (NC\_003071.7), *HsRBM3* and *HsCIRBP* from *H. sapiens* (NC\_000023.11 and NC\_000019.10, respectively). Amino acid positions within RRM that are identical in at least three proteins are highlighted in green (boxes indicate RNA contact regions RNP1 and RNP2). Glycine and arginine/glutamine residues in the glycine-rich region are labelled in red and blue, respectively.

**B** Hyphae of AB33 derivatives (6 h.p.i.). Growth direction and basal septa are marked by arrows and asterisks, respectively (scale bar, 10  $\mu\text{m}$ ).

**C** Hyphal length over time. Black and grey dots represent hyphae with and without septa, respectively. Shown are merged data (> 200 hyphae per strain) from three independent experiments, overlaid with the mean of means, red line and standard error of the mean (s.e.m.). Significance was assessed using paired two-tailed Student's *t*-test on the mean hyphal lengths from the replicate experiments, followed by multiple testing correction (Benjamini–Hochberg). Significant *P*-values ( $P < 0.05$ ) for comparison against wild type within each time point are indicated above.

**D** Length of empty sections (see Fig EV1J). Merged data from three independent experiments are shown together, overlaid with mean of means, red line and s.e.m. (total hyphae analysed: *wt*, 250; *grp1Δ*, 190; *grp1-gfp*, 332; difference in means between *wt* and *grp1-gfp* was statistically not significant, ns,  $P = 0.95$ ; paired two-tailed Student's *t*-test on the mean lengths from the replicate experiments ( $n = 3$ )).

**E** Differential interference contrast (DIC, top) and fluorescence images (bottom) of AB33 hyphae (5 h.p.i.) stressed at 3 h.p.i. with cell wall inhibitor CFW (2.5  $\mu\text{M}$ ). Arrowheads indicate aberrant cell wall deformation (scale bar, 10  $\mu\text{m}$ ).

**F** Percentage of hyphae with normal cell walls with (stressed) and without (unstressed) CFW treatment (data points represent percentages of three independent experiments,  $n = 3$ ; mean, dark grey lines and standard error of the mean, s.e.m., > 100 hyphae analysed per experiment; paired two-tailed Student's *t*-test on the means).

presence of *Rrm4*<sup>mR123</sup>-trf (Fig 2J). Thus, the localisation of Grp1 depends on the presence of functional Rrm4, more precisely on its capability to bind RNA. In summary, we identified Grp1 as a novel component of endosomal mRNPs whose shuttling on Rrm4-positive endosomes depended on Rrm4 and mRNA.

### Rrm4 and Grp1 share thousands of target transcripts

In order to learn more about the function of the two endosomal mRNP components Rrm4 and Grp1 during hyphal growth, we performed a comparative transcriptome-wide analysis of their RNA

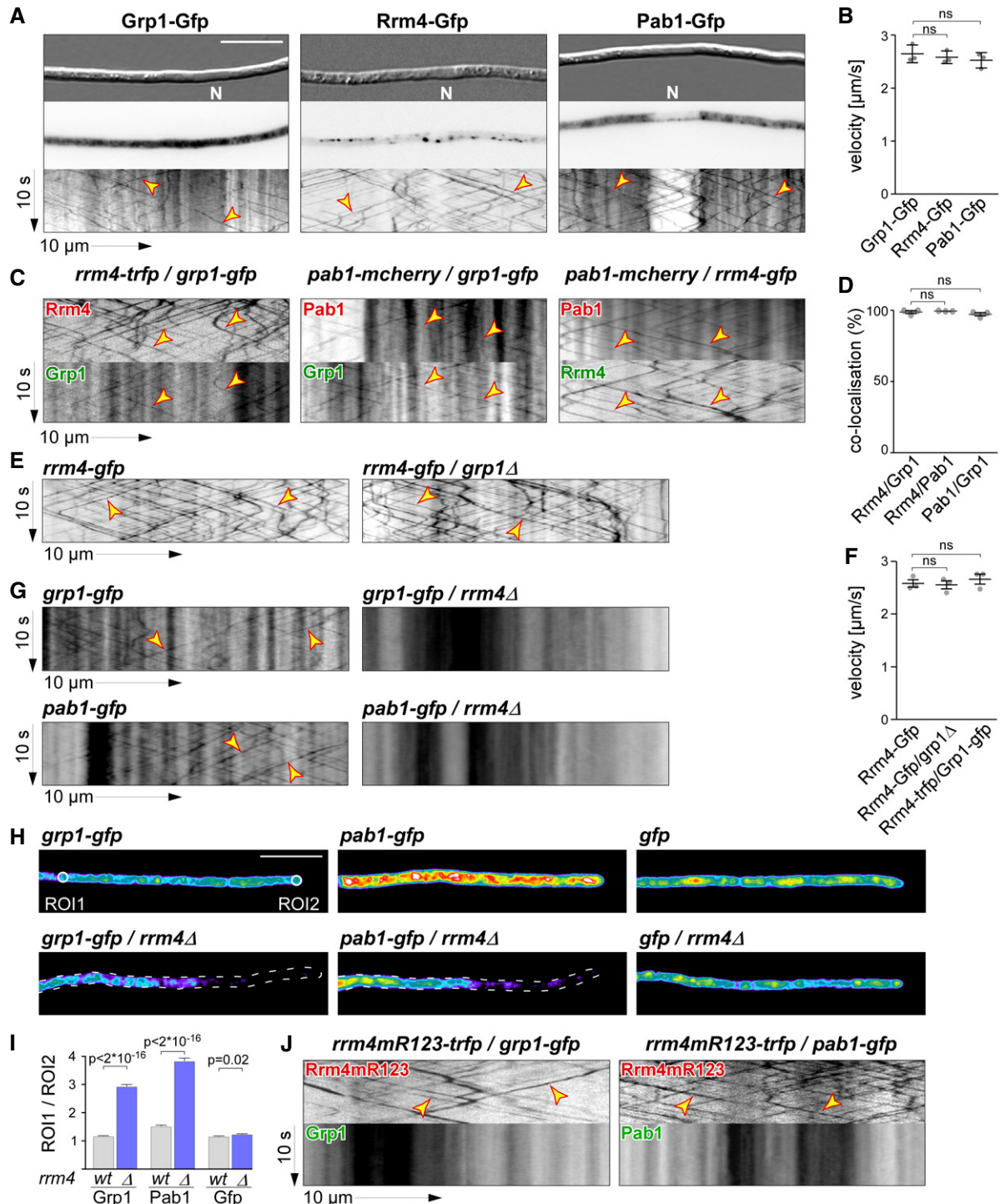


Figure 2.

binding behaviour using individual-nucleotide resolution UV crosslinking and immunoprecipitation (iCLIP) [29]. For application with fungal RBPs, we had to modify a number of steps in the iCLIP protocol (Fig EV2A–D; see Materials and Methods) [30]. One major challenge was the high RNase and protease activity in fungal cell extracts that resulted in a low yield of crosslinked protein-RNA complexes and short mRNA fragments. The most critical changes to

the protocol came with the fast processing of crosslinked material and the identification of the optimal UV-C irradiation dose (Fig EV2B).

Using the improved protocol, we found that Rrm4-Gfp and Grp1-Gfp displayed substantial crosslinking to RNA *in vivo* (compared to Gfp control; Fig 3A). As expected, the RNA signal was dependent on UV-C irradiation and sensitive to RNase I digestion. Upon iCLIP

**Figure 2. Grp1 shuttles on Rrm4-positive endosomes throughout hyphae.**

- A Micrographs (DIC and inverted fluorescence image; scale bar, 10  $\mu\text{m}$ ) and corresponding kymographs of AB33 hyphae (6 h.p.i.) expressing Grp1-Gfp, Rrm4-Gfp or Pab1-Gfp (arrow length on the left and bottom indicates time and distance, 10 s and 10  $\mu\text{m}$ , respectively). To visualise directed movement of signals (distance over time) within a series of images, kymographs were generated by plotting the position of signals along a defined path (x-axis) for each frame of the corresponding video (y-axis). Bidirectional movement is visible as diagonal lines (yellow arrowheads; N, nucleus; Video EV1). For an example image of a complete AB33 hypha, see Fig EV1A.
- B Average velocity of fluorescent signals per hypha for strains shown in (A) (movement of tracks with  $> 5 \mu\text{m}$  was scored as processive). Data points represent averages from three independent experiments ( $n = 3$ ), with mean, red line and s.e.m. At least 20 signals/hyphae were analysed out of 12 hyphae per experiment (ns;  $P = 0.18$  and  $P = 0.23$ ) using a paired two-tailed Student's *t*-test on the means.
- C Kymographs of hyphae of AB33 derivatives (6 h.p.i.) expressing pairs of red and green fluorescent proteins as indicated. Fluorescence signals were detected simultaneously using dual-view technology (arrow length as in A). Processive co-localising signals are marked by yellow arrowheads (Videos EV2–EV4).
- D Percentage of red fluorescent signals exhibiting co-localisation with the green fluorescent signal for strains shown in (C). Data points represent observed co-localisation in three independent experiments, mean, dark grey line and s.e.m. ( $n = 3$ , 11 hyphae each; paired two-tailed Student's *t*-test on the means; ns;  $P = 0.63$  and  $P = 0.5$ ).
- E Kymographs comparing hyphae of AB33 derivatives (6 h.p.i.) expressing Rrm4-Gfp in the wild type (left) or *grp1Δ* strains (right) (processive signals marked by yellow arrowheads; arrow length on the left and bottom indicates time and distance, 10 s and 10  $\mu\text{m}$ , respectively; Video EV5).
- F Average velocity of fluorescent signals per hyphae for strains shown in (E) (movement of tracks with  $> 5 \mu\text{m}$  were scored as processive). Data points represent averages from three independent experiments ( $n = 3$ ) with mean, black line and s.e.m. At least 20 signals/hypha were analysed out of at least 10 hyphae per experiment (ns;  $P = 0.27$  and  $P = 0.4$ ) using a paired two-tailed Student's *t*-test on the means.
- G Kymographs comparing hyphae (6 h.p.i.) expressing Grp1-Gfp or Pab1-Gfp in wild type (left) with *rrm4Δ* strains (right; processive signals marked by yellow arrowheads; arrow length as in A).
- H Hyphal tips (4 h.p.i.) of AB33 derivatives expressing Grp1-Gfp, Pab1-Gfp or Gfp alone comparing wild type (top) with *rrm4Δ* strains (bottom). Fluorescence micrographs in false colours (black/blue to red/white, low to high intensities, respectively; scale bar, 10  $\mu\text{m}$ ; ROI1 and ROI2-labelled circles exemplarily indicate regions of interest analysed in E).
- I Ratio of signal intensities in strains shown in (H) comparing Gfp fluorescence at the tip (ROI1) and in close vicinity to the nucleus (ROI2; see Materials and Methods). Bars represent mean and s.e.m. (*wt*:  $n = 160$ ; *rrm4Δ*:  $n = 152$ ), Pab1G ( $n = 126$ ; *rrm4Δ*:  $n = 170$ ), Gfp ( $n = 152$ ; *rrm4Δ*:  $n = 210$ ), unpaired two-tailed Student's *t*-test.
- J Kymographs of hyphae of AB33 derivatives (6 h.p.i.) expressing pairs of red and green fluorescent proteins as indicated (arrow length as in A; Videos EV6 and EV7). Fluorescence signals were detected simultaneously using dual-view technology. Processive co-localising signals are marked by yellow arrowheads. Note that processive movement is completely lost in the lower panels. Only static signals, visualised as vertical lines, are remaining.

library preparation, we obtained more than 100 million sequencing reads, corresponding to  $4.7 \times 10^6$  and  $14.8 \times 10^6$  crosslink events for Rrm4 and Grp1, respectively (Fig EV3A and B). Reproducibility between two replicate experiments was high for both proteins, demonstrating the quality of the obtained dataset (Pearson correlation coefficient  $> 0.96$ ,  $P$ -value  $< 2.22\text{e-}16$ ; Fig EV3C).

Consistent with the abundance of both proteins, the crosslink events accumulated into thousands of clusters that spread across major parts of the transcriptome (Fig EV3A). In order to focus on the most prominent sites, we used the crosslink frequency within each cluster relative to the background signal within the same transcript to determine the 25% most prominent binding sites for Rrm4 and Grp1 (“signal-over-background”; see Materials and Methods). This procedure identified a total of 6,412 binding sites for Rrm4 and 6,478 binding sites for Grp1, residing in 3,262 and 3,165 target transcripts, respectively (Fig 3B). This represented a substantial fraction of the about 6,700 protein-encoding genes in the *U. maydis* genome [31]. Extensive endosomal transport of mRNA is consistent with a role in evenly distributing mRNAs throughout hyphae (see Discussion).

Comparing Rrm4 and Grp1 revealed a large overlap of 2,114 target transcripts that were conjointly bound by both proteins (Fig 3B and C, Dataset EV1; see below). In this shared target set, we observed an enrichment for functional categories like mitochondrion, vesicle transport and cytoskeleton (Fig 3D). Moreover, we found several known Rrm4 target transcripts, including for instance all four septin mRNAs (Fig 3C and E). Binding sites of Rrm4 and Grp1 in the septin mRNAs were almost exclusively located in the 3' untranslated region (UTR), consistent with the hypothesis that these mRNAs are transported in a translationally active state (see Discussion) [19]. *cts1* mRNA, another known target of the Rrm4 transport

machinery [18], also carried binding sites of both RBPs in the 3' UTR (Fig EV3D).

To assess the function of target mRNAs that are specifically recognised by only one of the two RBPs, we applied more stringent criteria to define 280 and 520 transcripts that were uniquely bound by Rrm4 and Grp1, respectively (Fig EV3E, Datasets EV2 and EV3). While the Rrm4-unique set displayed no clear trend, the Grp1-unique set showed an enrichment for mRNAs encoding nuclear proteins that were involved in transcriptional regulation and chromatin remodelling (Fig 3D). Although these mRNAs were expressed and bound by Grp1, they were most likely not transported by the Rrm4 machinery, which we presume would result in perinuclear localisation. This could facilitate an efficient nuclear import of the translation products, as being described in mammalian cells for transcription factors like c-Myc or for metallothionein [32,33].

In summary, the comparative iCLIP approach revealed that Grp1 and Rrm4 conjointly bind thousands of shared target mRNAs. These offer a comprehensive view on the full spectrum of cargo mRNAs transported by the endosomal mRNA transport machinery in *U. maydis*.

**Rrm4 binds to functionally important sites of target transcripts**

Studying the distribution of binding sites in different transcript regions revealed that Rrm4 and Grp1 preferentially bound in the 3' UTR (Fig 4A). Within this region, both proteins frequently bound in close proximity, with 51% of Rrm4 binding sites directly overlapping with a Grp1 binding site (compared to only 5% in the open reading frame, ORF; Fig 4B and C). Thus, the cargo mRNAs of the transport mRNPs are often conjointly recognised by both RBPs in the 3' UTR.

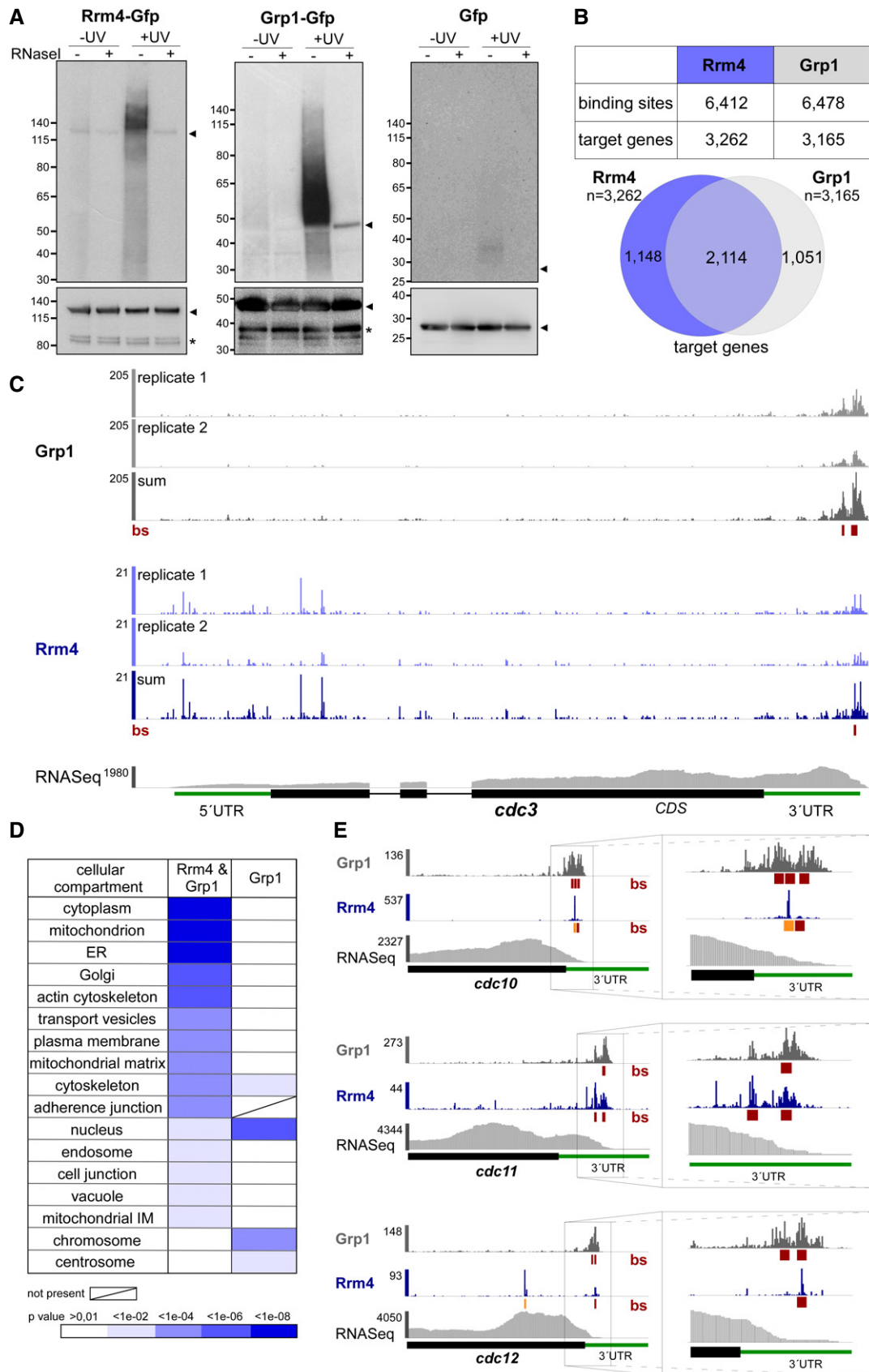


Figure 3.

**Figure 3. Rrm4 and Grp1 bind to thousands of target transcripts.**

- A Autoradiograph and Western blot analyses for representative iCLIP experiments with Rrm4-Gfp, Grp1-Gfp and Gfp. Upper part: Upon radioactive labelling of co-purified RNAs, the protein-RNA complexes were size-separated in a denaturing polyacrylamide gel. Protein-RNA complexes are visible as smear above the size of the protein (Rrm4-Gfp, 112 kDa; Grp1-Gfp, 45 kDa; Gfp, 27 kDa; indicated by arrowheads on the right). Samples with and without UV-C irradiation and RNase I (see Materials and Methods) are shown. Lower part: corresponding Western blot analysis using  $\alpha$ -Gfp antibody (arrowheads and asterisks indicate expected protein sizes and putative degradation products, respectively).
- B Summary of binding sites and target transcripts of Rrm4 and Grp1 (top). Venn diagram (below) illustrates the overlap of Rrm4 and Grp1 target transcripts.
- C iCLIP data for Rrm4 and Grp1 on *cdc3* (UMAG\_10503; crosslink events per nucleotide from two experimental replicates [light grey/light blue] and merged data [grey/blue] from AB33 filaments, 6 h.p.i.). Track below the merged iCLIP data shows binding sites for each protein (bs, red). Note that crosslink events in the 5' UTR and first exon of *cdc3* were not assigned as binding sites due to low reproducibility between replicates (see Materials and Methods). RNASeq coverage from wild type AB33 filaments (6 h.p.i.) is shown for comparison. Gene model with exon/intron structure below was extended by 300 nt on either side to account for 5' and 3' UTRs (green).
- D Functional categories of cellular components (FunCat annotation scheme, 78) for proteins encoded by target transcripts that are shared between Rrm4 and Grp1 (left) or unique to Grp1 (right). *P*-values for the enrichment of the listed category terms are depicted by colour (see scale below).
- E iCLIP data (crosslink events from merged replicates) for Rrm4 (blue) and Grp1 (grey) as well as RNASeq coverage on selected target transcripts (*cdc10*, UMAG\_10644; *cdc11*, UMAG\_03449; *cdc12*, UMAG\_03599). Enlarged regions (indicated by boxes) of the 3' UTR (green) are shown on the right. Datasets and visualisation as in (C). Binding sites (bs) are shown (red; orange indicates overlap with UAUG).

In contrast to Grp1 that was almost exclusively attached to the 3' UTR, Rrm4 bound a substantial fraction of target mRNAs within the ORF (1,315 mRNAs with 1,783 ORF binding sites; Fig 4A and C). Taking a closer look at the binding pattern of Rrm4 along ORFs, we observed binding sites at the start and stop codons of a subset of target mRNAs, reflected in increased crosslinking of Rrm4 at these sites (Fig 4D). Whereas only two transcripts harboured a Grp1 binding site at the start codon, Rrm4 binding sites overlapped the start codon in 47 target mRNAs, like in the transcript encoding the translation initiation factor Sui1 (UMAG\_02665; Fig EV3D; Dataset EV4). Of note, the *rrm4* mRNA itself exhibited Rrm4 binding sites around the start codon, hinting at a potential autoregulation (Fig 4E).

Even more prominently than at start codons, we observed a strong accumulation of Rrm4 binding sites at the stop codons of multiple target transcripts (291 cases; Fig 4D and E; Dataset EV5). These included, for example, both subunits of cytoplasmic dynein (Dyn1 and Dyn2) [34]. Furthermore, the stop codon-bound targets were significantly enriched for mRNAs encoding mitochondrial proteins, including for instance the majority of nucleus-encoded subunits and accessory components of the F<sub>1</sub>F<sub>0</sub>-ATPase (Fig EV4A–C). Through binding at the stop codon, Rrm4 might influence translation termination for these targets. This hypothesis was supported by revisiting data from a previous proteomics approach analysing the membrane-associated proteome of wild type and *rrm4Δ* hyphae, in which the amount of the membrane-associated component Atp4 was threefold reduced in *rrm4Δ* hyphae compared to wild type (Fig EV4D) [18].

In essence, the high-resolution mapping of binding sites for the two endosomal RBPs Rrm4 and Grp1 revealed (i) that both proteins conjointly bind in the 3' UTR and (ii) that Rrm4 additionally recognises binding sites in the ORF and at start and stop codons.

**Rrm4 specifically recognises the motif UAUG via its third RRM**

In order to address the RNA sequence specificity of both RBPs, we used the motif analysis algorithm DREME [35] to search for sequence motifs in a 30-nt window around the RBP binding sites. This analysis retrieved UAUG as the most significantly enriched sequence motif at Rrm4 binding sites (Fig 5A). Analysing the relative positioning of the motif showed that more than one-third of all

Rrm4 binding sites harboured a UAUG motif precisely at the centre of the binding site (2,201 out of 6,412; Fig 5B). The motif did not accumulate at Grp1 binding sites, supporting the notion that the motif was specifically recognised by Rrm4. In order to estimate the relative strength of Rrm4 binding, we calculated the “signal-over-background” (SOB), i.e. the ratio of crosslink events within the binding site over the background of crosslink events in the surrounding sequence (see Materials and Methods). The background binding served as a proxy for the abundance of underlying transcript. Since the SOB procedure did not correct for UV crosslinking biases and similar confounding factors, comparisons between binding sites were only performed at a global scale. We observed that the Rrm4 binding sites with UAUG showed stronger relative binding than those lacking the motif (Fig 5C), suggesting a tight interaction of Rrm4 with the UAUG-associated binding sites.

A similar sequence analysis of the Grp1 binding sites initially suggested the sequence UGUA as a potential recognition motif (Fig EV5A). However, the same motif also frequently occurred at Rrm4 binding sites and showed no clear positioning relative to the Grp1 binding sites (Fig EV5B), making it questionable whether it was directly involved in the RNA recognition of Grp1. We therefore did not pursue this motif further.

In order to independently test whether Rrm4 specifically recognises the sequence motif UAUG, we applied the yeast three-hybrid assay (Fig 5D). We previously used this approach to successfully identify SELEX-derived RNA aptamers that were recognised by the third RRM domain of Rrm4 *in vivo* (RRM3) [36]. Intriguingly, two RNA aptamers, SELEX-A1 and SELEX-B1, contained the UAUG motif. We chose SELEX-A1 (Fig 5E) [36] to mutate the UAUG motif and tested RNA binding using the yeast three-hybrid assay. In contrast to the initial SELEX-A1 aptamer, the mutant version was no longer recognised by Rrm4 (Figs 5F and EV5C). Consistent with earlier results, mutating the third RRM domain of Rrm4 gave similar results in the context of the initial SELEX-A1 aptamer [36]. Thus, our computational and experimental analyses indicate that Rrm4 specifically recognises the sequence motif UAUG via its third RRM domain.

Interestingly, Rrm4 binding sites in the whole ORF region showed a strong enrichment for the Rrm4 motif UAUG (Fig 5G), such that 61% of all ORF binding sites harboured UAUG. Since the start codon AUG is contained within this motif, the vast majority of

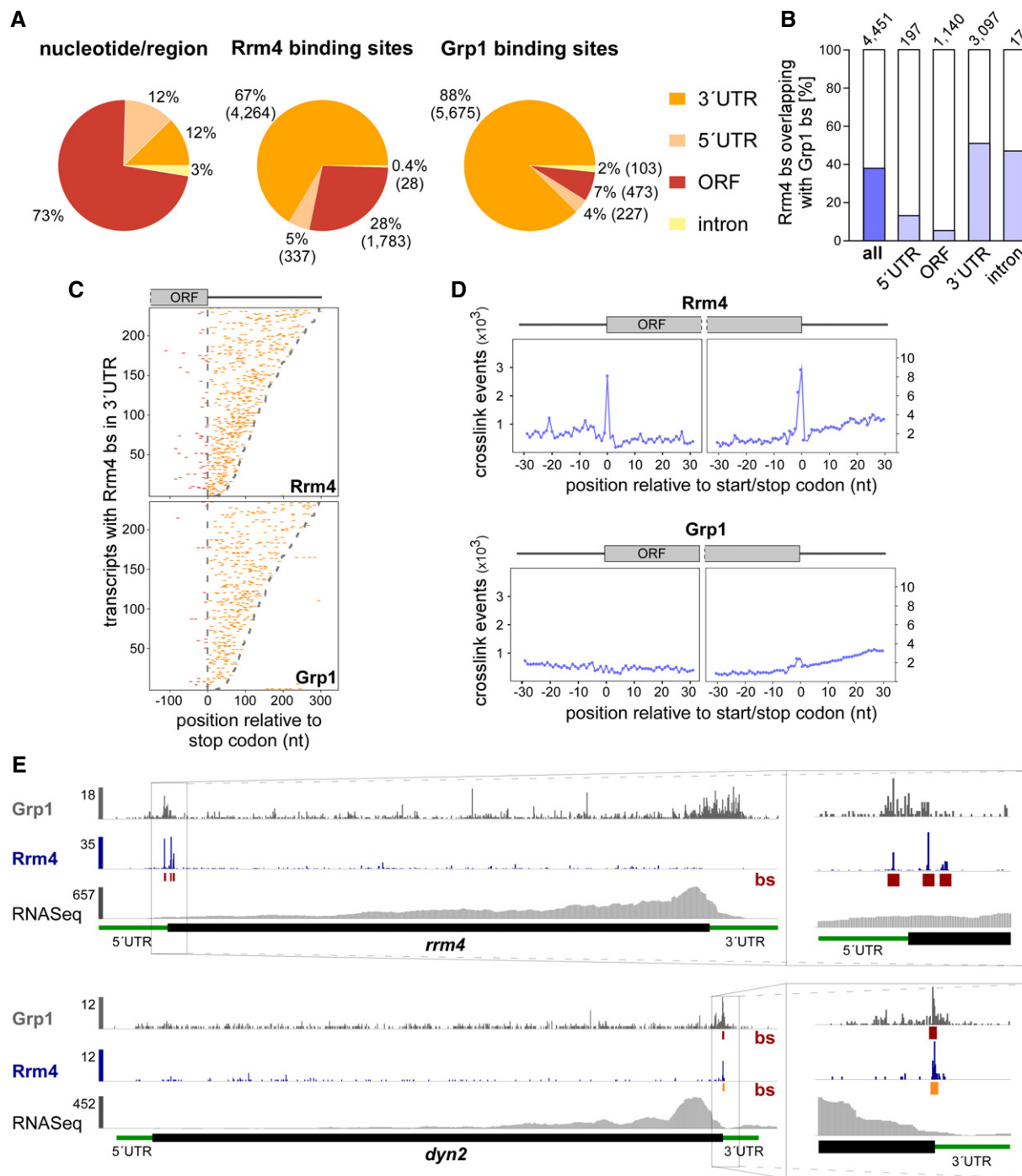


**Figure 4. Rrm4 binds target transcripts at the start and stop codons.**

A Distribution of binding sites within different transcript regions: 5' UTR, 3' UTR, ORF and intron. Percentage and absolute number of binding sites are given for each category. On the left, a transcriptome-wide distribution of nucleotides per transcript region is shown for comparison.

B Percentage of Rrm4 binding sites (bs) overlapping with Grp1 bs (by at least 1 nt) within shared target transcripts, shown for all bs and separated into transcript regions. The total number of binding sites per category is indicated on top.

C Positional maps of Rrm4 (top) and Grp1 (bottom) bs relative to the stop codon (position 0). Binding sites in ORFs and 3' UTR are given in red and orange, respectively. 234 target transcripts were randomly selected carrying an Rrm4 bs in the 3' UTR (with > 100 Rrm4 crosslink events; out of 1,715 Rrm4/Grp1 shared targets with Rrm4 bs in 3' UTR; Dataset EV6). Transcripts were ordered by decreasing 3' UTR length (see Materials and Methods).

D Metaprofiles of Rrm4 (top) and Grp1 (bottom) crosslink events relative to the start and stop codons (position 0). Note that crosslink events are substantially more frequent towards ORF ends, reflected in different y-axis scales.

E Genome browser views of Rrm4 and Grp1 iCLIP events as well as RNASeq data of *sui1* (UMAG\_02665) and *dyn2* (UMAG\_04372). Visualisation as in Fig 3C.



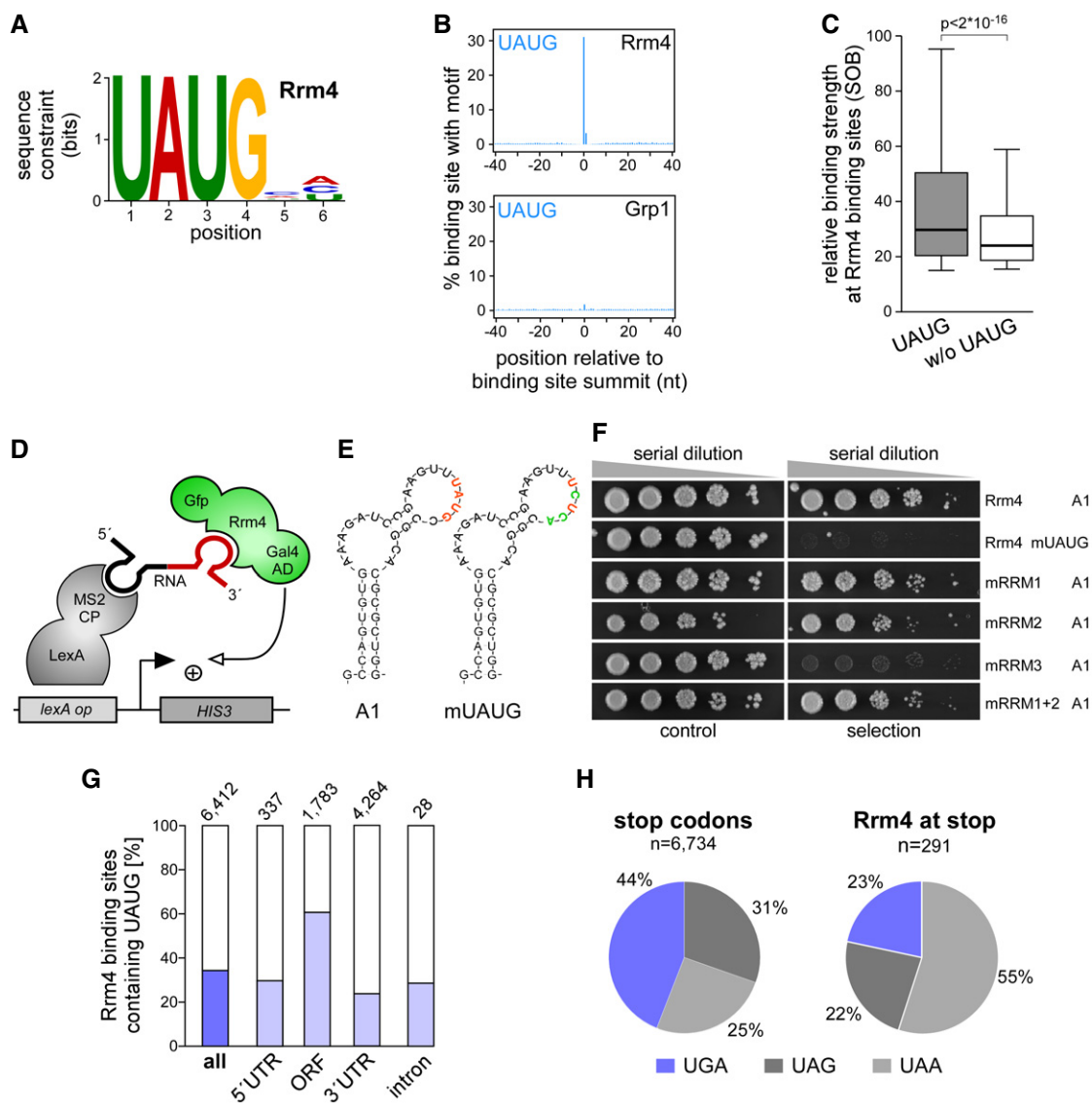


**Figure 5. Rrm4 recognises UAUG *in vivo*.**

- A** Logo representation of the most enriched sequence motif at Rrm4 binding sites. At each position, the height of the stack is proportional to the information content, while the relative height of each nucleotide within the stack represents its relative frequency at this position.
- B** Frequency of the Rrm4 motif UAUG around Rrm4 and Grp1 binding sites. Shown is the percentage of binding sites that harbour an UAUG starting at a given position in an 81-nt window around the binding site summit.
- C** Box plot comparing relative binding strength at Rrm4 binding sites (signal-over-background, SOB; see Materials and Methods) with or without UAUG ( $n = 2,201$  and  $n = 4,211$ , respectively; unpaired Student's *t*-test). Box limits represent quartiles, centre lines denote 50<sup>th</sup> percentiles, and whiskers extend to most extreme values within 1.5 $\times$  interquartile range.
- D** Schematic representation of the yeast three-hybrid system: *lexA operator* (*lexA op*) sequences are bound by the LexA-MS2 coat protein (CP) hybrid (grey), recruiting the MS2-SELEX-RNA hybrid (black and red, respectively) to the promoter region of the *HIS3* reporter gene. Transcription is activated by binding of the third hybrid AD-Rrm4-Gfp (green) carrying a Gal4 activation domain (AD).
- E** RNA structure prediction of aptamer SELEX-A1 with UAUG (red) or the mutated version mUAUG containing UCUC(A) (mutated bases in green).
- F** Colony growth on control and selection plates of yeast cells expressing protein and RNA hybrids indicated on the right. RNA binding is scored by growth on selection plates (SC -his +3-AT, 3-amino-1,2,4-triazole). mRRMx, Rrm4 variants harbouring mutations in RRM1, 2, 3 or 1 and 2.
- G** Percentage of Rrm4 bs containing the motif UAUG, shown for all bs and separated into transcript regions. The total number of binding sites is indicated on top.
- H** Relative contribution of the three stop codon variants to all (left) and Rrm4-bound stop codons (right). Although opal stop codons (UGA) fit best with a UAUG-containing binding site (UAUGA; present at 32 out of 63 bound UGA stop codons, 51%), they are depleted from Rrm4-bound stop codons.

start codon-associated binding sites exhibited the UAUG motif (88%, Fig EV5D). However, the frequency of Rrm4 binding was not increased compared to UAUG motifs in the surrounding sequence,

indicating that Rrm4 does not show a particular preference for UAUG motifs in the context of translational start sites (Fig EV5E). Nevertheless, the Rrm4 recognition motif intrinsically overlaps with

the start codon, suggesting a potential link to translation regulation. Binding of Rrm4 at the start codon might interfere, for example, with translational initiation of the bound target mRNAs.

In contrast to the UAUG prevalence in the ORF, stop codons seem to be recognised differently (UGA overlaps with UAUG, i.e. UAUGA; but UAA was the most common stop codon, 55%, Fig 5H). Since UAUG-containing binding sites showed particularly strong Rrm4 binding (Fig 3C; as example, see *cdc12* in Fig 3E), Rrm4 appears to exhibit a tight association with the ORF via its third RRM domain. Uniting these observations, we hypothesised that Rrm4 simultaneously recognised multiple regions of the same cargo mRNAs. In line with this notion, we found that transcripts with a Rrm4 binding site in the 3' UTR were significantly enriched for a second Rrm4 binding site in the ORF (663 out of 1,703 transcripts with at least two Rrm4 binding sites;  $P$ -value < 2.22e-16, Fisher's exact test). In 69% of these cases, the ORF binding site harboured UAUG and in 56%, the 3' UTR binding site of Rrm4 overlapped with a Grp1 binding site. Taken together, these observations would be consistent with a model that Rrm4 binds with its RRM domains RRM1 and/or RRM2 close to Grp1 in the 3' UTR and via its third RRM domain to a UAUG-containing binding site in the ORF (Fig 6).

## Discussion

At present, a small number of high-throughput studies provide a global view on transported and localised mRNAs. In oocytes and embryos from fruit fly, transcriptome-wide RNA *in situ* hybridisation approaches revealed that the majority of transcripts exhibit a defined localisation pattern [37,38]. In neuronal cells, the localised transcriptome and proteome have also been compiled [39,40]. However, it is still unclear (i) how these cargo mRNAs reach their destination, (ii) which RBPs mediate their transport and (iii) what are the precise interaction sites within the target mRNAs. Here, we applied iCLIP to study the newly identified endosomal RBP Grp1 and the key transport RBP Rrm4 during endosomal mRNA transport in *U. maydis*. To the best of our knowledge, this is the first detailed iCLIP analysis of mRNA transport.

### The GQ-rich RNA-binding protein Grp1 is a novel component of endosomal mRNPs

The small GQ-rich protein Grp1 shares similarity with other glycine-rich RBPs from humans and plants. A characteristic feature of this conserved class of RBPs is an N-terminal RRM domain followed by a glycine-rich low-complexity sequence that is typical for intrinsically disordered regions (IDRs). In RBPs, IDRs can mediate the assembly of membrane-less organelles through phase transitions [41], and this assembly is important, for example, during splicing [42]. Interestingly, IDRs have also been implicated in the formation of RNA granules for neuronal RNA transport [43,44].

Small glycine-rich RBPs function in a wide variety of biological processes. The plant protein *AtGRP7*, for example, is involved in cold stress adaptation, osmotic stress response, circadian rhythm and plant immunity [21,45,46]. Human CIRBP regulates telomerase activity, and the human cold-shock protein RBM3 is involved in translational reprogramming during the cooling response of

neuronal cells [20,47,48]. Globally, these proteins might function as RNA chaperones that prevent the formation of aberrant RNA secondary structures under stress conditions [45,49].

In this study, we observe that loss of the fungal orthologue Grp1 causes aberrant alterations of the hyphal growth programme. Under optimal conditions, *grp1Δ* hyphae grow significantly longer, suggesting an unusual acceleration of cell wall formation. Moreover, cell wall stress revealed clear abnormal morphologies in comparison with wild type. Consistent with a role in hyphal growth, Grp1 shuttles on Rrm4-positive endosomes that are the main transport units for long-distance transport of mRNAs in hyphae. Moreover, Grp1 and Rrm4 conjointly bind in the 3' UTRs of thousands of target mRNAs (Fig 6A, see below). We therefore propose that the potential RNA chaperone Grp1 most likely constitutes an accessory component of endosomal mRNPs. Its function could be particularly important under suboptimal conditions. Alternatively, Grp1 might regulate stability and/or translation of mRNAs encoding proteins involved in hyphal growth independent of endosomal mRNA transport.

It is of note that the RRM protein Hrb27C (Hrp48) from fruit fly with a related domain architecture containing two N-terminal RRMs followed by a C-terminal GQ-rich region was found as an mRNA component during transport of *oskar* and *gurken* mRNAs [50–52]. Hence, the presence of small glycine-rich RBPs in transport mRNPs might be preserved across organisms.

### Endosomal RBPs recognise a broad spectrum of cargo mRNAs

In order to obtain a comprehensive view on the *in vivo* mRNA targets of an RBP, UV crosslinking techniques are currently the method of choice [53–55]. Here, we applied iCLIP to study fungal mRNA transport. A strength of our approach was the use of strains expressing functional Gfp-tagged versions of Grp1 and Rrm4 using homologous recombination to avoid overexpression artefacts. For application in fungi, we had to improve several steps [30], of which optimising the dose and duration of UV-C irradiation was most critical. Thereby, we were able to obtain a transcriptome-wide view of the cargo mRNAs, including their interaction sites with cognate RBPs at single nucleotide resolution.

Comparing two distinct RBPs present in endosomal mRNPs enabled us to disentangle the precise binding behaviour of the two co-localising RBPs. We identified more than 2,000 shared target transcripts, covering a substantial amount of the approximately 6,700 annotated protein-coding genes [31]. The broad target spectrum of endosomal mRNA transport fits with earlier observations that Rrm4 transported all mRNAs under investigation, albeit with different processivity of transport [17]. Moreover, loss of Rrm4 impairs the global mRNA distribution in hyphae, indicated by a disturbed subcellular distribution of the poly(A)-binding protein Pab1 [17]. Thus, one function of the endosomal mRNA transport machinery might be the equal distribution of mRNPs to supply all parts of the hyphae with mRNAs. This might be particularly important for those parts that are distant from the mRNA-synthesising nucleus. Such a universal mRNA transport mode resembles the “sushi belt model” in neuronal cells, in which the shuttling of mRNPs by active transport along microtubules is thought to distribute mRNAs throughout the dendrite to serve synapses that are in demand of mRNAs [56]. Furthermore, since many mRNAs in

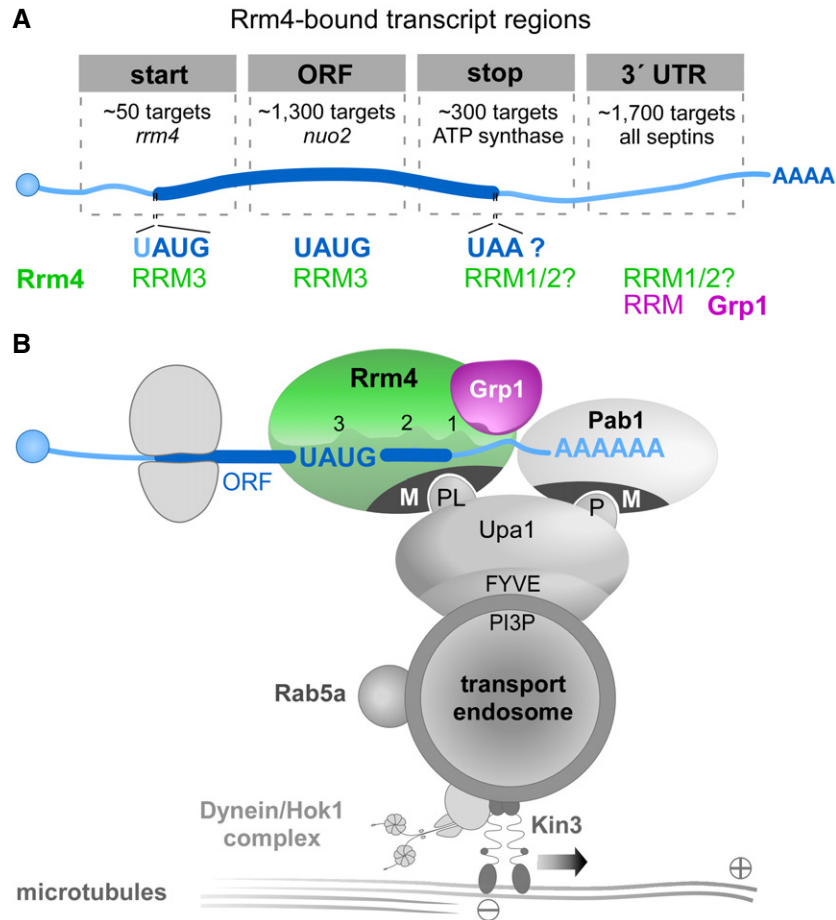


**Figure 6. Model of Rrm4-/Grp1-mediated endosomal mRNA transport.**

- A Schematic drawing of target transcript with Rrm4-bound regions on top (5' cap structure, blue circle; 5' and 3' UTR, light blue; ORF, dark blue; poly(A) tail, AAAAA). Different categories of Rrm4 target transcripts were defined according to the presence of Rrm4 binding sites at the start codon, within the ORF, at the stop codon and in the 3' UTR. Approximate number of target transcripts and selected examples are given for each category. About 900 of 1,300 target transcripts with an Rrm4 binding site in the ORF harbour a UAUG motif within the ORF binding site. Potential RRM domains of Rrm4 and Grp1 that may mediate RNA binding in the different transcript regions are given in green and magenta, respectively.
- B Simplified model proposing the spatial arrangement of endosomal RBPs with bound target transcripts. The three RRM domains of Rrm4 are schematically displayed and labelled by numbers (FYVE zinc finger domain; PI3P, phosphatidylinositol 3-phosphate; M, Mademoiselle domain; P and PL, PAM2 and PAM2-like sequence, respectively; further details, see text). Note that complete endosomal mRNPs will consist of additional mRNA and protein components forming more complex, higher order structures.

*U. maydis* appear to be transported in a translationally active state (see below), this mRNA distributor function would also disclose the mechanism of how ribosomes are transported by endosomes, as observed previously [57].

Notably, we found that most nucleus-encoded subunits and accessory components of mitochondrial  $F_1F_0$ -ATPase are targets of endosomal mRNA transport in *U. maydis*. Consistent with the idea that a precise spatiotemporal regulation of translation might be important for efficient mitochondrial protein import, we observed that the abundance of Atp4 is reduced in *rrm4Δ* hyphae [18]. These results agree with previous findings that the 3' UTR of *ATP2* mRNA from *S. cerevisiae* is important for efficient mitochondrial uptake of mature Atp2p [58]. A close link between RNA biology and mitochondrial protein import is thus an emerging theme in mitochondrial biology [59–63].

### Distinct binding patterns of Rrm4 may allow orchestration of mRNA transport and translation

The positional information obtained by single nucleotide resolution was essential to uncover the precise binding behaviour of the involved RBPs. In the majority of cases, Rrm4 binds together with Grp1 in the 3' UTR (1,700 transcripts; Fig 6A). The vicinity of these binding sites to the poly(A) tail fits the previous observation that the endosomal adaptor protein Upa1 interacts with both Rrm4 and Pab1 [64]. While translating ribosomes would potentially remove RBPs from the ORF [65], such binding in the 3' UTR, as seen, e.g., on all four septin mRNAs, would allow simultaneous translation and transport of mRNAs. Consistently, we have recently provided evidence that endosome-coupled translation of septin mRNAs mediates endosomal assembly and transport of heteromeric septin

complexes [6,19]. Since transport of translationally active mRNAs has recently been observed in neurons [66], this mode of transport might be more widespread than currently anticipated.

Our transcriptome-wide RNA binding maps illustrate an intriguing binding pattern of Rrm4 at translational landmark sites, indicating an intimate connection of endosomal mRNA transport and translation in *U. maydis* (Fig 6A): First, in over 1,000 target transcripts Rrm4 binds within the ORF, indicating that it may be involved in stalling translational elongation. Notably, a similar mechanism was suggested in neurons, in which a subset of mRNAs are translationally stalled during transport [67]. Similar to Rrm4, the neuronal RBP FMR1 binds its translationally stalled target mRNAs preferably in the coding sequence [68]. Second, in about 50 and 300 target transcripts, respectively, Rrm4 precisely binds at the start and stop codons, suggesting modulation of translation initiation and termination. At start codons and within the ORF, the Rrm4 binding sites frequently harboured UAUG. This motif is recognised by the third RRM domain of Rrm4. In accordance with its ELAV-type domain organisation, we therefore propose that Rrm4 binds UAUG-containing binding sites via its third RRM to influence translation (Fig 6B), while the two tandem RRMs (RRM1/2) bind the target mRNAs in the 3' UTR, possibly together with Grp1 (Fig 6B). In a previous study, we observed that mutations in RRM1 and RRM3 led to strongly reduced overall RNA binding of Rrm4, although mutations in RRM3 did not show a mutant phenotype with respect to hyphal growth [16]. In contrast, mutations in RRM1 strongly affected hyphal growth [16], accompanied by reduced endosomal shuttling of Pab1 as well as *cdc3* mRNA [6]. Therefore, the potential translational regulation during endosomal mRNA transport mediated by RRM3 may be an additive and used for fine-tuning. The tandem RRM domains RRM1 and RRM2 of Rrm4 might mediate the recognition of target mRNAs for transport, possibly via binding in the 3' UTR.

In essence, our comprehensive transcriptome-wide view on endosomal mRNA transport revealed the precise positional deposition of co-localising RBPs during transport. The key RBP Rrm4 exhibits a particular binding behaviour by recognising distinct landmarks of translation in target mRNAs. Thereby, translation and transport might be intimately coupled and precisely synchronised for the specific expression needs of each target transcript.

## Materials and Methods

### Plasmids, strains and growth conditions

Cloning was done using *E. coli* K-12 derivative Top10 (Life Technologies, Carlsbad, CA, USA). All strains were constructed by the transformation of cells with linearised plasmids and homologous integration events were verified by Southern blot analysis [69]. Genomic DNA of wild type strain UM521 (*a1b1*) served as template for PCR amplifications unless noted otherwise. Proteins were tagged with eGfp (enhanced green fluorescent protein; Clontech, Mountain View, CA, USA), tagRfp or mCherry [26,70]. Plasmid sequences are available upon request. The accession numbers of *U. maydis* genes used in this study are as follows: *rrm4* (UMAG\_10836), *grp1* (UMAG\_02412), *pab1* (UMAG\_03494). Detailed information is supplied in Appendix Tables S1–S3. The conditions used for

cultivation of *U. maydis* are described elsewhere [69]. For the induction of filamentous growth of laboratory strain AB33 and derivatives, cultures were grown to an OD<sub>600</sub> of 0.5 in complete medium supplemented with 1% glucose (CM-glc) and shifted to nitrate minimal medium supplemented with 1% glc (NM-glc). The growth curves of *U. maydis* strains were recorded by cultivating strains in CM-glc at 28°C and measuring the OD<sub>600</sub> every 2 h.

### Multiple sequence alignments

Orthologous proteins were identified using BLAST P (<https://blast.ncbi.nlm.nih.gov/blast/>). Clustal W and GeneDoc 2.6 were used for multiple amino acid sequence alignment and graphical representation, respectively [71].

### Preliminary affinity purification experiments using Rrm4-GfpTT as bait

Preliminary purification experiments were performed using a strain expressing Rrm4 fused C-terminally to Gfp and tandem affinity purification (TAP) tag [16]. We analysed the eluted fractions by mass spectrometry either as complex mixture in solution (Fig EV1C) or by cutting individual bands from an SDS-PAGE (Fig EV1D). In both cases, the protein purification followed a published protocol (CLIP) [16]. Both experiments were considered to be pilot studies and were only performed once. In case of the in-solution digest, the protein samples were precipitated with 20% trichloroacetic acid (1:2, v/v) and washed five times with cold acetone. Samples were digested with sequencing-grade modified trypsin (Promega), and the resulting peptides were separated into fractions by nanoLC (PepMap100 C-18 RP nanocolumn and UltiMate 3000 liquid chromatography system, Dionex). Fractions were spotted with matrix solution on a MALDI plate and subsequently analysed by MALDI-TOF MS (4800 Proteomics Analyser, AB Sciex). Mass spectrometry data were searched against the MUMDB (Munich *Ustilago Maydis* Data Base; 6,785 entries; IBIS Institute of Bioinformatics and Systems, German Research Center for Environmental Health) [31] using Mascot embedded into GPS Explorer software (AB Sciex). The total peptide score is the sum of all peptide scores corresponding to the predicted proteins, excluding the scores of duplicate matches. The best peptide score is the best score from all identified peptides corresponding to the predicted proteins.

Applying as filter a total peptide score of larger than 46, we identified 23 proteins as potential interaction partners of Rrm4 (Fig EV1C). Among these proteins were interesting candidates that were identified before in independent approaches: Chitinase Cts1 and ribosomal protein Rps19 were found in a differential proteomics study, comparing wild type and *rrm4Δ* hyphae [18]. Upa2 is a PAM2 motif-containing protein that was identified as potential interaction partner of Rrm4 in a bioinformatics approach [64]. Grp1 (UMAG\_02412) was chosen for further analysis, since it contained an RNA recognition motif (RRM) for RNA binding.

In the gel-based approach, the calmodulin beads were washed three times and incubated in SDS-loading buffer for 8 min at 90°C. The supernatant was subjected to SDS-PAGE (10% polyacrylamide). Proteins were stained with Coomassie blue. After excision of selected bands, samples were destained and dried under vacuum. The dried material was suspended in 30 μl 10 mM ammonium

bicarbonate (pH 8.3) containing 0.6 µg of trypsin (Promega) and 10% acetonitrile. After incubation at room temperature for 12 h, the trypsin digest was extracted and analysed as described above. We were able to verify Rrm4-GfpTT (TEV cleavage product 117 kDa) and Grp1 (18 kDa; Fig EV1D) in selected bands matching their expected gel position after electrophoresis.

### Colony morphology, temperature stress and cell wall stress

For growth on solid media, cell suspensions (OD<sub>600</sub> of 0.5) were inoculated onto respective plates at 28°C. Colony morphology was tested on CM (1% glc) medium. Temperature stress was analysed on CM (1% glc) medium, incubated at 28°C, 20°C or 16°C. Cell wall stress was analysed by supplementing CM (1% glc) medium with 50 µM calcofluor-white (Sigma-Aldrich, Taufkirchen, Germany) or 40 µg/ml Congo red (Sigma-Aldrich). All plates were kept for at least 48 h at the required temperature. The set-up used to acquire images was described before [64]. To analyse cell wall stress in hyphae, 2.5 µM calcofluor-white was added to cultures 3 hours post-induction (h.p.i) and incubated for an additional 2 h.

### Microscopy and image processing

The microscope set-ups and dual-colour imaging were used as described before [5,25,72]. Gfp and tagRfp or mCherry fluorescence was simultaneously detected using a two-channel imager (DV2, Photometrics, Tucson, AZ, USA). All images and videos were acquired and analysed using Metamorph (Versions 7.7.0.0 and 7.7.4.0; Molecular Devices, Sunnyvale, CA, USA).

Cell length was assessed by measuring the length of single cells from pole to pole. For hyphae, empty sections were not included in the measurements. The length of empty sections was assessed by measuring the distance from septum to septum of the first empty section at the distal pole of hyphae. Cell wall defects induced by calcofluor-white were quantified by manually scoring for the presence of abnormal cell wall shapes.

For the analysis of co-localisation and velocity of moving signals the acquired videos were converted to kymographs using Metamorph. Co-localisation was assessed by quantifying kymographs acquired by dual-colour imaging. Changes in direction were counted as individual signals. Processive signals (distance travelled > 5 µm) were counted manually. Velocity was only measured for processive signals (movement > 5 µm). For all quantifications, at least three independent experiments were analysed. Statistical analysis was performed using Prism5 (GraphPad, La Jolla, CA, USA).

The gradient of Grp1-Gfp, Pab1-Gfp and Gfp in the presence and absence of Rrm4 was quantified by measuring the fluorescence intensity in a previously specified region of interest (ROI; ROI1 in vicinity to the nucleus and ROI2 at the hyphal tip). The fluorescence close to the nucleus was then set in relation to the signal intensity at the tip. Statistical analysis was performed using Prism5 (GraphPad, La Jolla, CA, USA).

### iCLIP experiments

The iCLIP protocol was modified from [30] and the original application in *U. maydis* [17]. (i) The initial two-step TAP-tag purification [17] was switched to single-step purification using strains

expressing C-terminal Gfp fusions and Gfp-trap immunoprecipitation (GFP-Trap\_MA, ChromoTek, Martinsried, Germany) [73]. (ii) For UV-C crosslinking, cells were irradiated continuously in a single session. (iii) The addition of DNase and RNase I was omitted from the samples used for iCLIP library preparation. Due to the high RNase activity in fungal cells, the addition of external RNases was unnecessary; therefore, RNase I (10 units/sample; 16 min, 37°C; Thermo Fisher Scientific, Darmstadt, Germany) was only added in the control experiments (Fig 3A).

All iCLIP experiments were performed with 150 ml cultures grown to an OD<sub>600</sub> = 0.5 in CM (1% glc) and then shifted to NM-medium (1% glc) to induce hyphal growth. After 6 h, each culture was split into 3 × 50 ml, harvested by centrifugation at 6,280 g for 10 min at 4°C and the cell pellets were resuspended in 5 ml ice-cold PBS. For UV-C crosslinking, cells were irradiated once with 200 mJ/cm<sup>2</sup> at 254 nm (Biolink UV-Crosslinker, Vilber-Lourmat, Eberhardzell, Germany) as a thin layer in a square Petri dish (10 cm<sup>2</sup>), pooled in a 50-ml tube, and harvested by centrifugation at 6,280 g for 10 min at 4°C. The cell pellet was resuspended in 6 ml lysis buffer (50 mM Tris-HCl, pH 7.4, 100 mM NaCl, 1% Nonidet P-40, 0.1% SDS, 0.5% sodium deoxycholate) supplemented with inhibitors (per 10 ml lysis buffer): 2× Complete protease inhibitor EDTA-free (Roche Diagnostics, Mannheim, Germany), 1 mM reduced DTT (GERBU, Heidelberg, Germany), 5 mM benzamidine (Sigma), 1 mM PMSF (Sigma), 0.75 µg/µl heparin (Sigma), 5.25 ng/µl pepstatin A (Sigma) and 15 µl SUPERase-In (20 U/µl; Thermo Fisher Scientific). The solution was split into three times 2 ml for cell lysis and immunoprecipitation. Cell lysis was performed in a Retsch ball mill (2 ml cell suspension/grinding jar, 2 grinding balls, d = 12 mm; MM400; Retsch, Haan, Germany) 3 × 10 min at 30 Hz while keeping samples frozen using liquid nitrogen. All of the following steps up to the 5' labelling of RNA were performed at 4°C. The cell lysates were pooled in a 15-ml tube, split in precooled 1.5-ml tubes and cleared by centrifugation at 16,200 g for 15 min at 4°C. The protein-RNA complexes were immunoprecipitated from each strain by using a total of 60 µl GFP-Trap magnetic agarose beads (Chromotek; GFP-Trap\_MA) [73]. Before immunoprecipitation, 60 µl beads were added to a 2 ml tube and pre-washed three times with 500 µl ice-cold lysis buffer (without inhibitors) and afterwards split into three times 20 µl beads in 2 ml tubes. For immunoprecipitation, 2 ml cleared cell lysate was added to 20 µl beads and the tubes were incubated rotating for 1 h at 4°C. Next, the beads were combined in a 2 ml tube and washed three times with 900 µl high-salt wash buffer (50 mM Tris-HCl, pH 7.4, 1 M NaCl, 1 mM EDTA, 1% IGEPAL CA-630, 0.1% SDS, 0.5% sodium deoxycholate) and four times with 900 µl PNK wash buffer (20 mM Tris-HCl, pH 7.4, 10 mM MgCl<sub>2</sub>, 0.2% Tween-20). For each subsequent enzymatic reaction, 60 µl beads were split into three times 20 µl beads in 2 ml tubes and re-pooled for the washing steps. 3' end RNA dephosphorylation, L3 adapter ligation, 5' end phosphorylation, SDS-PAGE and nitrocellulose transfer were performed as described [30] with minor changes implemented. For 5' end phosphorylation, 50% of each sample was radioactively labelled with <sup>32</sup>P-γ-ATP for 10 min at 37°C and the labelled beads were washed once with PNK wash buffer before they were combined with the unlabelled beads. The beads were diluted in 80 µl NuPAGE LDS loading buffer (Thermo Fisher Scientific) with 0.1 M DTT added. Samples

were heated at 70°C for 5 min and split among two adjacent wells on a 4–12% NuPAGE Bis-Tris gel (Thermo Fisher Scientific). The protein-RNA complexes were separated at 180 V for 70 min in MOPS running buffer with NuPAGE reducing agent added (Thermo Fisher Scientific) and transferred onto a nitrocellulose membrane. For Western blotting, Gfp was detected using monoclonal  $\alpha$ -GFP primary antibodies (clones 7.1 and 13.1; Sigma) and a mouse IgG HRP conjugate (H+L; Promega, Madison, WI, USA) as secondary antibody. Peroxidase activity was determined using the AceGlow blotting detection system (Peqlab, Erlangen, Germany).

Labelled RNA was detected by exposure of X-ray films ranging from 2 h to overnight at –80°C. cDNA library preparation was performed as described before [30]. To avoid over-amplification of the cDNA library, the optimal number of PCR cycles producing PCR products of around 150 nt (cDNA insert = 20–30 nt; L3 adapter, RT-primer and P3/P5 Solexa primers = 128 nt) was tested for each protein in every experiment (PCR cycler PTC-200, MJ Research, St. Bruno, Quebec, Canada; Fig EV2D). For all Grp1 and Gfp replicates, 18 PCR cycles were determined to be optimal, while the optimal PCR cycle numbers for the Rrm4 replicates were determined to be 18 and 22 PCR cycles. The iCLIP libraries were multiplexed and sequenced on an Illumina HiSeq 2500 (San Diego, CA, USA; 51-nt reads, single-end), yielding a total of 118 million reads.

### iCLIP data processing

All bioinformatics analyses are based on the *U. maydis* 521 genome sequence (original PEDANT database name p3\_t237631\_Ust\_maydi\_v2GB) and the associated gene annotation (version p3\_t237631\_Ust\_maydi\_v2GB.gff3; both downloaded from ftp://ftp.mips.gsf.de/fungi/Ustilaginaceae/Ustilago\_maydis\_521/). We extended all genes by 300 nt on either side to include potential 5' and 3' UTR regions which are currently not annotated in the *U. maydis* genome. For manual annotation of transcript ends, RNASeq data (AB33 hyphae, 6 h.p.i.) were used, and transcript ends were defined at the position where read coverage dropped below 10.

Basic quality checks were applied to all sequenced reads using FastQC (<https://www.bioinformatics.babraham.ac.uk/projects/fastqc/>). Afterwards, iCLIP reads were filtered based on sequencing quality (Phred score) in the barcode region, keeping only reads with at most one position with a Phred score < 20 in the experimental barcode (positions 4–7) and without any position with a Phred score < 17 in the random barcode (positions 1–3 and 8–9). The reads were then de-multiplexed based on the experimental barcode at positions 4–7 using Flexbar (version 2.4, GitHub, San Francisco, CA, USA) without allowing mismatches [74]. The following analysis steps were applied to all individual samples: remaining adapter sequences were trimmed from the 3' end of the reads using Flexbar (version 2.4) allowing one mismatch in 10 nt, requiring a minimal overlap of 1 nt between read and adapter as well as removing all reads with a remaining length of less than 24 nt (including the 9-nt barcode). The first 9 nt of each read containing the barcode was trimmed off and added to the read name in the fastq file.

Filtered and trimmed reads were mapped to the *U. maydis* genome and its gene annotation using STAR (version 2.5.1b, GitHub) [75], allowing up to two mismatches and without soft-clipping on

the 5' end of the reads. Only uniquely mapped reads were kept for further analysis.

After mapping and filtering, duplicate reads were marked using the *dedup* function from bamUtil (version 1.0.7; <https://github.com/statgen/bamUtil>) and removed if carrying an identical random barcode, and hence representing technical duplicates. The nucleotide position upstream of each aligned read was considered as the “crosslink nucleotide”, with each read counted as individual “crosslink event”. The total number of crosslink events for the different iCLIP libraries can be found in Fig EV3A. To assess the reproducibility between biological replicates (Fig EV3C), we counted the number of crosslink events within each gene.

We then proceeded to define putative RBP “binding sites”, i.e. sites that show a significant enrichment of crosslink events compared to the surrounding sequence. Since most RBPs contact multiple positions in the RNA, the crosslink events in a binding site commonly spread across more than one nucleotide. For the identification of such windows with significantly increased crosslink event frequency, peak calling was performed using ASPeak that accounts for the different expression levels of the underlying transcripts [76]. Peak calling was performed on merged replicates for each RBP to maximise the signal. In order to obtain binding sites of a uniform width, we further processed the predicted peaks [77]. We first determined the summit of each peak (i.e. the position with highest number of crosslink events within the peak; if two or more positions showed the same count, the most upstream position was taken) and then defined a binding site window of 9 nt that was centred around the summit position. Overlapping peaks were merged and newly centred on the summit of the combined window as described above. Finally, we filtered the binding sites as follows: (i) To account for reproducibility, we required each binding site to be detected by at least 5 crosslink events from each biological replicate. (ii) We further removed all Rrm4 and Grp1 binding sites that overlapped by at least 1 nt with any of 88 reproducible Gfp binding sites. To define the set of target genes that were exclusively bound by Rrm4 and showed no evidence of Grp1 binding (“Rrm4-unique targets”), we subtracted the intermediate list of binding sites at this point for Grp1 from the final Rrm4 binding sites (after SOB filtering, see below), and vice versa.

For the remaining analysis, we included an additional processing step to focus on the top 25% of binding sites. To determine this set, we used the ratio of crosslink events within the binding site over the background crosslink events in the surrounding sequence (termed “signal-over-background”, SOB) as a proxy of binding site strength: crosslink events from both replicates were summed up within each binding site and divided by the gene-specific background to obtain an SOB value for each binding site. The background for each gene was defined as the number of crosslink events outside the binding sites divided by the number of nucleotides in the gene that harbour such background crosslink events. We note that while this procedure alleviates the impact of transcript-level differences, it does not correct for UV crosslinking bias and similar confounding factors, and should therefore only be used as a proxy for bulk comparisons of binding sites. Only binding sites within the top 25% of the SOB distribution for each RBP were taken into consideration for further analyses.

This SOB filtering procedure yielded a total of 6,412 and 6,478 binding sites for Rrm4 and Grp1, respectively (Figs 3B and EV3).

The binding sites corresponded to 3,262 and 3,165 target transcripts for Rrm4 and Grp1, respectively. When assigning genomic nucleotides and RBP binding sites to distinct transcript regions (Fig 3D), we applied the following hierarchy to resolve overlapping annotation: 3' UTR > 5' UTR > exon > intron. Binding sites of Rrm4 and Grp1 were considered as overlapping if at least 1 nt was shared between the 9-nt binding sites.

To study the distribution of binding sites of Rrm4 and Grp1 in 3' UTRs (Fig 4C), we manually annotated transcript ends. This was necessary, because the *U. maydis* gene annotation only includes ORF regions of genes. To this end, RNASeq data from AB33 hyphae (6 h.p.i.) were visually inspected and 3' ends were defined due to strong reduction in RNASeq coverage.

Enriched sequence motifs around RBP binding sites were identified using DREME [35]; parameter `-norc` to search the coding strand only) to analyse a 30-nt window around all binding site summits compared to shuffled nucleotides. Based on the sequence profile and the UAUG content around binding sites (Fig 5A and B), we counted a binding site as UAUG-containing if it harboured the motif with the last 5 nt of the 9-nt binding sites. In order to assess the frequency of Rrm4 binding sites at UAUG motifs at start codons and in other regions (Fig EV5E), we used all transcripts that carry Rrm4 binding sites anywhere within the transcript and are hence sufficiently expressed to be detected in our iCLIP analysis.

Analysing functional categories of cellular components on identified targets was performed using the FunCat annotation scheme (<http://mips.gsf.de/funecatDB/>; version 2.1, reference genome: p3\_t237631\_Ust\_maydi\_v2GB) [78]. Categories were filtered during analysis for enrichment by setting the *P*-value threshold to < 0.05.

### RNASeq library preparation and data processing

RNA was extracted from AB33 hyphae 6 h.p.i. using the RNeasy Mini Kit following the manufacturer's instructions for preparation of total RNA from yeast (Qiagen, Hilden, Germany). To this end, AB33 hyphae were opened in a Retsch ball mill (3 balls, d = 4 mm; MM400; Retsch, Haan, Germany) 4 times for 5 min at 30 Hz while keeping samples frozen using liquid nitrogen. The resulting cell powder was resolved in 450 µl RLT buffer (+β-mercaptoethanol) and centrifuged at 16,200 g for 2 min at 4°C. The supernatant was transferred to a new reaction tube, mixed with 1 volume 70% EtOH and then added to the RNeasy spin column. All following processing steps were performed according to manufacturer's instructions. TruSeq RNA Library Prep kit v2 (Illumina, San Diego, CA, USA) was used for cDNA library generation. The cDNA libraries were sequenced using the HiSeq 2000 platform (Illumina) with 151-nt single-end reads.

Basic quality checks were applied to all sequenced reads using FastQC (<https://www.bioinformatics.babraham.ac.uk/projects/fastqc/>). Afterwards, RNASeq reads were trimmed based on sequencing quality (Phred score) using Flexbar (version 3.0.3) [74]. Specifically, adapter sequences were removed (TruSeq Universal Adapter), and reads were trimmed at the first position with a Phred score < 20 and removed if the remaining read length was less than 20 nt. The trimmed reads were mapped to the *U. maydis* genome and its gene annotation using STAR (version 2.5.3a) [75], allowing up to five mismatches with soft-clipping. Uniquely mapped reads were kept for further analysis.

### Yeast three-hybrid analysis

Yeast three-hybrid experiments were performed as described previously [36,79]. To test the interaction with Rrm4, the plasmids (Appendix Table S4) encoding the RNA aptamers SELEX-A1 [36] or mutated SELEX-A1 (mUAUG; this work) were cotransformed in strain L40 coat with the corresponding plasmids encoding for Rrm4 or mutated variants [36,80]. Transformed cells were incubated on SC -ura -leu plates (2–3 days at 28°C) before single clones were selected. Interaction was assayed as growth on selection medium SC -his +1 mM 3-AT (3-amino-1,2,4-triazole; Sigma-Aldrich; 3 days at 28°C). For the serial dilution assays, single clones were grown in SC -ura -leu medium to a starting OD<sub>600</sub> = 0.5 and sequentially diluted 1:5 in water. The dilutions were then spotted on control (SC -ura -leu) and selection (SC -his +1 mM 3-AT) plates and incubated at 28°C.

### Data availability

The iCLIP and RNASeq dataset are available from GEO under the accession numbers GSE109557 and GSE109560, respectively. The associated SuperSeries is GSE109561.

**Expanded View** for this article is available online.

### Acknowledgements

We thank Dr. J. Kahnt for pilot TAP-tag experiments and Dr T. Pohlmann for initial work on Grp1 fusion proteins. We acknowledge R.F.X. Sutandy for iCLIP support, M. Brüggemann for RNASeq data analysis, F. Finkernagel for bioinformatics and Dr. M. Seiler for critical reading of the manuscript. We are grateful to U. Gengenbacher and S. Esch for excellent technical assistance and members of the IMB Genomics core facility for technical assistance. The work was funded by grants from the Deutsche Forschungsgemeinschaft to MF (FE 448/8-1; FOR2333-TP03 FE448/10-1; CEPLAS EXC1028) KZ (FOR2333-TP10 ZA881/1-1) JK (SPP1935 KO4566/2-1) and JU (European Research Council; 617837-Translate).

### Author contributions

LO, CH, JU, JKön, MF and KZ designed this study and analysed the data. LO and CH performed experiments to characterise Grp1 and comparative iCLIP analysis. JKoe performed preliminary affinity purification experiments. SB, AB and KZ performed all computational iCLIP data analyses. MF and KZ drafted and revised the manuscript with input from all co-authors. MF and KZ directed the project.

### Conflict of interest

The authors declare that they have no conflict of interest.

### References

- Holt CE, Bullock SL (2009) Subcellular mRNA localization in animal cells and why it matters. *Science* 326: 1212–1216
- Martin KC, Ephrussi A (2009) mRNA localization: gene expression in the spatial dimension. *Cell* 136: 719–730
- Eliscovich C, Singer RH (2017) RNP transport in cell biology: the long and winding road. *Curr Opin Cell Biol* 45: 38–46
- Mofatteh M, Bullock SL (2017) SnapShot: subcellular mRNA localization. *Cell* 169: 178.e1

5. Baumann S, Pohlmann T, Jungbluth M, Brachmann A, Feldbrügge M (2012) Kinesin-3 and dynein mediate microtubule-dependent co-transport of mRNPs and endosomes. *J Cell Sci* 125: 2740–2752
6. Baumann S, König J, Koepke J, Feldbrügge M (2014) Endosomal transport of septin mRNA and protein indicates local translation on endosomes and is required for correct septin filamentation. *EMBO Rep* 15: 94–102
7. Egan MJ, McClintock MA, Reck-Peterson SL (2012) Microtubule-based transport in filamentous fungi. *Curr Opin Microbiol* 15: 637–645
8. Steinberg G (2014) Endocytosis and early endosome motility in filamentous fungi. *Curr Opin Microbiol* 20: 10–18
9. Guimaraes SC, Schuster M, Bielska E, Dagdas G, Kilaru S, Meadows BR, Schrader M, Steinberg G (2015) Peroxisomes, lipid droplets, and endoplasmic reticulum “hitchhike” on motile early endosomes. *J Cell Biol* 211: 945–954
10. Salogiannis J, Egan MJ, Reck-Peterson SL (2016) Peroxisomes move by hitchhiking on early endosomes using the novel linker protein PxdA. *J Cell Biol* 212: 289–296
11. Salogiannis J, Reck-Peterson SL (2016) Hitchhiking: a non-canonical mode of microtubule-based transport. *Trends Cell Biol* 27: 141–150
12. Haag C, Pohlmann T, Feldbrügge M (2017) The ESCRT regulator Did2 maintains the balance between long-distance endosomal transport and endocytic trafficking. *PLoS Genet* 13: e1006734
13. Haag C, Steuten B, Feldbrügge M (2015) Membrane-coupled mRNA trafficking in fungi. *Annu Rev Microbiol* 69: 265–281
14. Vollmeister E, Feldbrügge M (2010) Posttranscriptional control of growth and development in *Ustilago maydis*. *Curr Opin Microbiol* 13: 693–699
15. Becht P, Vollmeister E, Feldbrügge M (2005) Role for RNA-binding proteins implicated in pathogenic development of *Ustilago maydis*. *Eukaryot Cell* 4: 121–133
16. Becht P, König J, Feldbrügge M (2006) The RNA-binding protein Rrm4 is essential for polarity in *Ustilago maydis* and shuttles along microtubules. *J Cell Sci* 119: 4964–4973
17. König J, Baumann S, Koepke J, Pohlmann T, Zarnack K, Feldbrügge M (2009) The fungal RNA-binding protein Rrm4 mediates long-distance transport of *ubi1* and *rho3* mRNAs. *EMBO J* 28: 1855–1866
18. Koepke J, Kaffarnik F, Haag C, Zarnack K, Luscombe NM, König J, Ule J, Kellner R, Begerow D, Feldbrügge M (2011) The RNA-binding protein Rrm4 is essential for efficient secretion of endochitinase Cts1. *Mol Cell Proteomics* 10: M111.011213
19. Zander S, Baumann S, Weidtkamp-Peters S, Feldbrügge M (2016) Endosomal assembly and transport of heteromeric septin complexes promote septin cytoskeleton formation. *J Cell Sci* 129: 2778–2792
20. Zhu X, Bührer C, Wellmann S (2016) Cold-inducible proteins CIRP and RBM3, a unique couple with activities far beyond the cold. *Cell Mol Life Sci* 73: 3839–3859
21. Kang H, Park SJ, Kwak KJ (2013) Plant RNA chaperones in stress response. *Trends Plant Sci* 18: 100–106
22. Brachmann A, Weinzierl G, Kämper J, Kahmann R (2001) Identification of genes in the bW/bE regulatory cascade in *Ustilago maydis*. *Mol Microbiol* 42: 1047–1063
23. Imai K, Noda Y, Adachi H, Yoda K (2005) A novel endoplasmic reticulum membrane protein Rcr1 regulates chitin deposition in the cell wall of *Saccharomyces cerevisiae*. *J Biol Chem* 280: 8275–8284
24. Ram AF, Klis FM (2006) Identification of fungal cell wall mutants using susceptibility assays based on Calcofluor white and Congo red. *Nat Protoc* 1: 2253–2256
25. Baumann S, Takeshita N, Grün N, Fischer R, Feldbrügge M (2015) Live cell imaging of endosomal trafficking in fungi. In *Methods in mol bio: membrane trafficking*, Tang BL (ed.), pp 347–363. New York, NY: Springer
26. Merzlyak EM, Goedhart J, Shcherbo D, Bulina ME, Shcheglov AS, Fradkov AF, Gaintzeva A, Lukyanov KA, Lukyanov S, Gadella TW et al (2007) Bright monomeric red fluorescent protein with an extended fluorescence lifetime. *Nat Methods* 4: 555–557
27. Campbell RE, Tour O, Palmer AE, Steinbach PA, Baird GS, Zacharias DA, Tsien RY (2002) A monomeric red fluorescent protein. *Proc Natl Acad Sci USA* 99: 7877–7882
28. Hogan DJ, Riordan DP, Gerber AP, Herschlag D, Brown PO (2008) Diverse RNA-binding proteins interact with functionally related sets of RNAs, suggesting an extensive regulatory system. *PLoS Biol* 6: e255
29. König J, Zarnack K, Rot G, Curk T, Kayikci M, Zupan B, Turner DJ, Luscombe NM, Ule J (2010) iCLIP reveals the function of hnRNP particles in splicing at individual nucleotide resolution. *Nat Struct Mol Biol* 17: 909–915
30. Huppertz I, Attig J, D’Ambrogio A, Easton LE, Sibley CR, Sugimoto Y, Tajnik M, König J, Ule J (2014) iCLIP: protein-RNA interactions at nucleotide resolution. *Methods* 65: 274–287
31. Kämper J, Kahmann R, Bölker M, Ma LJ, Brefort T, Saville BJ, Banuett F, Kronstad JW, Gold SE, Müller O et al (2006) Insights from the genome of the biotrophic fungal plant pathogen *Ustilago maydis*. *Nature* 444: 97–101
32. Chabanon H, Mickleburgh I, Burtle B, Pedder C, Hesketh J (2005) An AU-rich stem-loop structure is a critical feature of the perinuclear localization signal of c-myc mRNA. *Biochem J* 392: 475–483
33. Levadoux M, Mahon C, Beattie JH, Wallace HM, Hesketh JE (1999) Nuclear import of metallothionein requires its mRNA to be associated with the perinuclear cytoskeleton. *J Biol Chem* 274: 34961–34966
34. Straube A, Enard W, Berner A, Wedlich-Söldner R, Kahmann R, Steinberg G (2001) A split motor domain in a cytoplasmic dynein. *EMBO J* 20: 5091–5100
35. Bailey TL (2011) DREME: motif discovery in transcription factor ChIP-seq data. *Bioinformatics* 27: 1653–1659
36. König J, Julius C, Baumann S, Homann M, Göringer HU, Feldbrügge M (2007) Combining SELEX and yeast three-hybrid system for *in vivo* selection and classification of RNA aptamers. *RNA* 13: 614–622
37. Lécuyer E, Yoshida H, Parthasarathy N, Alm C, Babak T, Cerovina T, Hughes TR, Tomancak P, Krause HM (2007) Global analysis of mRNA localization reveals a prominent role in organizing cellular architecture and function. *Cell* 131: 174–187
38. Jambor H, Surendranath V, Kalinka AT, Mejsstrik P, Saalfeld S, Tomancak P (2015) Systematic imaging reveals features and changing localization of mRNAs in *Drosophila* development. *eLife* 4: e05003
39. Cajigas IJ, Tushev G, Will TJ, tom Dieck S, Fuerst N, Schuman EM (2012) The local transcriptome in the synaptic neuropil revealed by deep sequencing and high-resolution imaging. *Neuron* 74: 453–466
40. Rangaraju V, Tom Dieck S, Schuman EM (2017) Local translation in neuronal compartments: how local is local? *EMBO Rep* 18: 693–711
41. Calabretta S, Richard S (2015) Emerging roles of disordered sequences in RNA-binding proteins. *Trends Biochem Sci* 40: 662–672
42. Ying Y, Wang XJ, Vuong CK, Lin CH, Damianov A, Black DL (2017) Splicing activation by Rbfox requires self-aggregation through its tyrosine-rich domain. *Cell* 170: 312–323.e10
43. Jung H, Yoon BC, Holt CE (2012) Axonal mRNA localization and local protein synthesis in nervous system assembly, maintenance and repair. *Nat Rev Neurosci* 13: 308–324
44. Kato M, Han TW, Xie S, Shi K, Du X, Wu LC, Mirzaei H, Goldsmith EJ, Longgood J, Pei J et al (2012) Cell-free formation of RNA granules: low complexity sequence domains form dynamic fibers within hydrogels. *Cell* 149: 753–767



45. Ciuzan O, Hancock J, Pamfil D, Wilson I, Ladomery M (2015) The evolutionarily conserved multifunctional glycine-rich RNA-binding proteins play key roles in development and stress adaptation. *Physiol Plant* 153: 1–11
46. Meyer K, Koster T, Nolte C, Weinholdt C, Lewinski M, Grosse I, Staiger D (2017) Adaptation of iCLIP to plants determines the binding landscape of the clock-regulated RNA-binding protein AtGRP7. *Genome Biol* 18: 204
47. Peretti D, Bastide A, Radford H, Verity N, Molloy C, Martin MG, Moreno JA, Steinert JR, Smith T, Dinsdale D et al (2015) RBM3 mediates structural plasticity and protective effects of cooling in neurodegeneration. *Nature* 518: 236–239
48. Bastide A, Peretti D, Knight JR, Grosso S, Spriggs RV, Pichon X, Sbarrato T, Roobol A, Roobol J, Vito D et al (2017) RTN3 is a novel cold-induced protein and mediates neuroprotective effects of RBM3. *Curr Biol* 27: 638–650
49. Kim JS, Park SJ, Kwak KJ, Kim YO, Kim JY, Song J, Jang B, Jung CH, Kang H (2007) Cold shock domain proteins and glycine-rich RNA-binding proteins from *Arabidopsis thaliana* can promote the cold adaptation process in *Escherichia coli*. *Nucleic Acids Res* 35: 506–516
50. Yano T, Lopez de Quinto S, Matsui Y, Shevchenko A, Shevchenko A, Ephrussi A (2004) Hrp48, a *Drosophila* hnRNPA/B homolog, binds and regulates translation of oskar mRNA. *Dev Cell* 6: 637–648
51. Huynh JR, Munro TP, Smith-Litiere K, Lepesant JA, St Johnston D (2004) The *Drosophila* hnRNPA/B homolog, Hrp48, is specifically required for a distinct step in osk mRNA localization. *Dev Cell* 6: 625–635
52. Goodrich JS, Clouse KN, Schupbach T (2004) Hrb27C, Sqd and Otu cooperatively regulate *gurken* RNA localization and mediate nurse cell chromosome dispersion in *Drosophila* oogenesis. *Development* 131: 1949–1958
53. König J, Zarnack K, Luscombe NM, Ule J (2012) Protein-RNA interactions: new genomic technologies and perspectives. *Nat Rev Genet* 13: 77–83
54. Van Nostrand EL, Pratt GA, Shishkin AA, Gelboin-Burkhart C, Fang MY, Sundararaman B, Blue SM, Nguyen TB, Surka C, Elkins K et al (2016) Robust transcriptome-wide discovery of RNA-binding protein binding sites with enhanced CLIP (eCLIP). *Nat Methods* 13: 508–514
55. Zarnegar BJ, Flynn RA, Shen Y, Do BT, Chang HY, Khavari PA (2016) irCLIP platform for efficient characterization of protein-RNA interactions. *Nat Methods* 13: 489–492
56. Doyle M, Kiebler MA (2011) Mechanisms of dendritic mRNA transport and its role in synaptic tagging. *EMBO J* 30: 3540–3552
57. Higuchi Y, Ashwin P, Roger Y, Steinberg G (2014) Early endosome motility spatially organizes polysome distribution. *J Cell Biol* 204: 343–357
58. Margeot A, Blugeon C, Sylvestre J, Vialette S, Jacq C, Corral-Debrinski M (2002) In *Saccharomyces cerevisiae*, ATP2 mRNA sorting to the vicinity of mitochondria is essential for respiratory function. *EMBO J* 21: 6893–6904
59. Gehrke S, Wu Z, Klinkenberg M, Sun Y, Auburger G, Guo S, Lu B (2015) PINK1 and Parkin control localized translation of respiratory chain component mRNAs on mitochondria outer membrane. *Cell Metab* 21: 95–108
60. Gold VA, Chroszcicki P, Bragoszewski P, Chacinska A (2017) Visualization of cytosolic ribosomes on the surface of mitochondria by electron cryotomography. *EMBO Rep* 18: 1786–1800
61. Lesnik C, Golani-Armon A, Arava Y (2015) Localized translation near the mitochondrial outer membrane: an update. *RNA Biol* 12: 801–809
62. Zhang Y, Chen Y, Gucek M, Xu H (2016) The mitochondrial outer membrane protein MDI promotes local protein synthesis and mtDNA replication. *EMBO J* 35: 1045–1057
63. Sen A, Cox RT (2016) Clueless is a conserved ribonucleoprotein that binds the ribosome at the mitochondrial outer membrane. *Biol Open* 5: 195–203
64. Pohlmann T, Baumann S, Haag C, Albrecht M, Feldbrügge M (2015) A FYVE zinc finger domain protein specifically links mRNA transport to endosome trafficking. *eLife* 4: e06041
65. Halstead JM, Lionnet T, Wilbertz JH, Wippich F, Ephrussi A, Singer RH, Chao JA (2015) Translation. An RNA biosensor for imaging the first round of translation from single cells to living animals. *Science* 347: 1367–1671
66. Wu B, Elisovich C, Yoon YJ, Singer RH (2016) Translation dynamics of single mRNAs in live cells and neurons. *Science* 352: 1430–1435
67. Graber TE, Hebert-Seropian S, Khoutorsky A, David A, Yewdell JW, Lacaillle JC, Sossin WS (2013) Reactivation of stalled polyribosomes in synaptic plasticity. *Proc Natl Acad Sci USA* 110: 16205–16210
68. Darnell JC, Van Driesche SJ, Zhang C, Hung KY, Mele A, Fraser CE, Stone EF, Chen C, Fak JJ, Chi SW et al (2011) FMRP stalls ribosomal translocation on mRNAs linked to synaptic function and autism. *Cell* 146: 247–261
69. Brachmann A, König J, Julius C, Feldbrügge M (2004) A reverse genetic approach for generating gene replacement mutants in *Ustilago maydis*. *Mol Genet Genomics* 272: 216–226
70. Shaner NC, Campbell RE, Steinbach PA, Giepmans BN, Palmer AE, Tsien RY (2004) Improved monomeric red, orange and yellow fluorescent proteins derived from *Discosoma* sp. red fluorescent protein. *Nat Biotechnol* 22: 1567–1572
71. Larkin MA, Blackshields G, Brown NP, Chenna R, McGettigan PA, McWilliam H, Valentin F, Wallace IM, Wilm A, Lopez R et al (2007) Clustal W and Clustal X version 2.0. *Bioinformatics* 23: 2947–2948
72. Baumann S, Zander S, Weidtkamp-Peters S, Feldbrügge M (2016) Live cell imaging of septin dynamics in *Ustilago maydis*. In *Methods in Cell Biol: Septins*, Gladfite AS (ed), pp 143–159. Amsterdam, Netherlands: Elsevier Inc
73. Rothbauer U, Zolghadr K, Muyldermans S, Schepers A, Cardoso MC, Leonhardt H (2008) A versatile nanotrap for biochemical and functional studies with fluorescent fusion proteins. *Mol Cell Proteomics* 7: 282–289
74. Dodt M, Roehr JT, Ahmed R, Dieterich C (2012) FLEXBAR-flexible barcode and adapter processing for next-generation sequencing platforms. *Biology* 1: 895–905
75. Dobin A, Davis CA, Schlesinger F, Drenkow J, Zaleski C, Jha S, Batut P, Chaisson M, Gingeras TR (2013) STAR: ultrafast universal RNA-seq aligner. *Bioinformatics* 29: 15–21
76. Kucukural A, Ozadam H, Singh G, Moore MJ, Cenik C (2013) ASPeak: an abundance sensitive peak detection algorithm for RIP-Seq. *Bioinformatics* 29: 2485–2486
77. Sutandy FXR, Ebersberger S, Huang L, Busch A, Bach M, Kang HS, Fallmann J, Maticzka D, Backofen R, Stadler PF et al (2018) In vitro iCLIP-based modeling uncovers how the splicing factor U2AF2 relies on regulation by cofactors. *Genome Res* 28: 699–713
78. Ruepp A, Zollner A, Maier D, Albermann K, Hani J, Mokrejs M, Tetko I, Guldener U, Mannhaupt G, Münsterkötter M et al (2004) The FunCat, a functional annotation scheme for systematic classification of proteins from whole genomes. *Nucleic Acids Res* 32: 5539–5545
79. Vollmeister E, Haag C, Zarnack K, Baumann S, König J, Mannhaupt G, Feldbrügge M (2009) Tandem KH domains of Khd4 recognize AUACCC and are essential for regulation of morphology as well as pathogenicity in *Ustilago maydis*. *RNA* 15: 2206–2218
80. SenGupta DJ, Zhang B, Kraemer B, Pochart P, Fields S, Wickens M (1996) A three-hybrid system to detect RNA-protein interactions in vivo. *Proc Natl Acad Sci USA* 93: 8496–8501
81. Kozak M (2005) Regulation of translation via mRNA structure in prokaryotes and eukaryotes. *Gene* 361: 13–37